Holistic design and implementation of pressure-actuated cellular structures

B. Gramüller, H. Köke, C. Hühne
German Aerospace Center, Institute of Composite Structures and Adaptive Systems
E-Mail: benjamin.gramueller@dlr.de

Abstract

Providing the possibility to develop energy-efficient, lightweight adaptive components, Pressure-Actuated Cellular Structures (PACS) are primarily conceived for aeronautics applications. The realization of shape-variable flaps and even airfoils provides the potential to safe weight, increase aerodynamic efficiency and enhance agility. The herein presented holistic design process points out and describes the necessary steps for designing a real-life PACS structure, from the computation of truss geometry to the manufacturing and assembly. The already published methods for the form finding of PACS are adjusted and extended for the exemplary application of a variable-camber wing. The transfer of the form-finding truss model to a cross-sectional design is discussed. The end cap and sealing concept is described together with the implementation of the integral fluid flow. Conceptual limitations due to the manufacturing and assembly processes are discussed. The method's efficiency is evaluated by Finite Element Method (FEM). In order to verify the underlying methods and summarize the presented work a modular real-life demonstrator is experimentally characterized and validates the numerical investigations.

Nomenclature

α_{AoA}	[°]	Angle of attack
α_B	[°]	Angle beam pendulum
$\alpha_{\boldsymbol{k}}, \alpha_{h,i,j}$	[rad]	Hinge angles
$\Delta\alpha_{\boldsymbol{k}}, \Delta\alpha_{h,i,j}$	[rad]	Hinge distortion
$\Delta\alpha_{max}$	[°]	Global maximal hinge distortion
A_0	[mm²]	Overall cross sectional area
$A_{\boldsymbol{k}}$	[mm²]	Cross sectional area of cell side
$a_{\boldsymbol{k}}, a_{h,i,j}$	[mm]	Cell side length
β_1, β_2	[°]	Distortion of PACS edge cell
C_L	[-]	Lift coefficient
C_D	[-]	Drag coefficient
c_{CL}	[m]	Chord length of wing profile
$c_{\boldsymbol{k}}, c_{h,i,j,k}$	[Nmm]	Rotational hinge stiffness
$\Delta\alpha_{AoA}$	[°]	Change of angle of attack
$\Delta\beta$	[°]	Change of distortion of PACS edge cell
$\Delta\beta_{dev}$	[°]	Deviation of distortion of PACS edge cell
$\Delta\beta_{hys}$	[°]	Hysteresis of distortion of PACS edge cell
$\Delta e_{\boldsymbol{k}}$	[°]	Distance of effective hinge position to hinge chord line
Δm	[t]	Change of total mass of PACS
$\delta r_{p,\boldsymbol{k}}, \delta r_{g,\boldsymbol{k}}, \delta r_{pl,\boldsymbol{k}}, \delta r_{ad,\boldsymbol{k}}$	[rad]	Virtual displacement (translational)
$\delta u_{\boldsymbol{k}}$	[rad]	Virtual displacement (rotational)
D	[mm]	Diameter of cell's circumcircle
D_B	[mm]	Bolt diameter
d	[mm]	Depth of structure
E, E_1, E_2	[GPa]	Elastic modulus
F_C	[N]	Clamping force for seal
F_{op}	[N]	Operating force for seal
f	[-]	Pressure factor
$f_{c,\boldsymbol{k}}$	[Nmm]	Momentums
$f_{p,\boldsymbol{k}}, f_{g,\boldsymbol{k}}, f_{pl,\boldsymbol{k}}, f_{ad,\boldsymbol{k}}, f_{a,\boldsymbol{k}}, f_{l,\boldsymbol{k}}, f_{tot,\boldsymbol{k}}$	[N]	Forces
G_C	[mm]	Shear modulus of adhesive
h	[-]	Number of cell row
$I_{z,\boldsymbol{k}}$	[mm⁴]	Second moment of inertia (z-direction)
i	[-]	Number of cell
j	[-]	Number of hinge or cell side
κ	[-]	Reduction factor for seal design
$\kappa_{\boldsymbol{k}}$	[-]	Hinge curvature
k_A	[-]	Tightening factor for seal design
L	[N]	Aerodynamic lift force
l^*	[mm]	Maximum load bearing bonding length
m	[t]	Total mass of PACS
$M_{C,\boldsymbol{k}}(x)$	[Nmm]	Cell side momentum
$\zeta_{\boldsymbol{k}}$	[mm]	Radius of hinge intersection area
η, η_t	[%]	Deviation
n_1, n_2	[-]	Number of cells per cell row
θ	[rad]	Orientation of acceleration
ν_∞	[m²/s]	kinematic viscosity
$\dot{\Pi}_{c,\boldsymbol{k}}, \dot{\Pi}_{p,\boldsymbol{k}}, \dot{\Pi}_{g,\boldsymbol{k}}, \dot{\Pi}_{pl,\boldsymbol{k}}, \dot{\Pi}_{ad,\boldsymbol{k}}$	[N]	Energy potential
$p_{ad}, p_{int}, p_\infty, p_{\boldsymbol{k}}$	[MPa]	Pressure
p_{max}	[MPa]	Maximum cell pressure
ρ	[t/mm³]	Density
R, R_B	[MPa]	Material strength
Re	[-]	Reynolds number
$r_{\boldsymbol{k}}$	[mm]	Hinge radius
$\sigma_{a,\boldsymbol{k}}, \sigma_{b,\boldsymbol{k}}, \sigma_{CS}$	[MPa]	Stresses
σ_{max}	[MPa]	Global maximal structural stress
σ_{vM}	[MPa]	Equivalent stress
SF, SF_{CS}	[-]	Safety factors
$s_{\boldsymbol{k}}$	[mm]	Hinge length
$\tau^*_{C,max}$	[MPa]	Maximum adhesive shear stress
T_∞	[k]	Ambient temperature
$t_{\boldsymbol{k}}$	[mm]	Thickness of flexure hinge
t_C	[mm]	Thickness of adhesive film
$t_{C,\boldsymbol{k}}(x)$	[mm]	Thickness of cell side at position x
t_{opt}	[mm]	Optimal thickness for flexure hinge
v	[m/s]	Airspeed
ν_∞	[m²/s]	kinematic viscosity
$\xi_{\boldsymbol{k}}$	[m/s]	Hinge orientation
$\partial W_{c,\boldsymbol{k}}, \partial W_{p,\boldsymbol{k}}, \partial W_{g,\boldsymbol{k}}, \partial W_{pl,\boldsymbol{k}}, \partial W_{ad,\boldsymbol{k}}$	[Nmm]	Virtual work
ψ	[-]	Ratio of longitudinal stiffness
$\boldsymbol{X}_{\boldsymbol{k}}, \boldsymbol{X}_{h,i,j}$	[mm]	Hinge position vector
$\ddot{x}$	[mm/s²]	Acceleration

1 Introduction

Biologically inspired technical solutions provide outstanding opportunities regarding the development and enhancement of materials, mechanisms, surfaces, sensors and structures. With the immense variety of the flora and fauna, an almost unlimited supply of well-tried ideas and technical concepts is available. A long-lasting, highly promising issue of aeronautical engineering, shape-variable structures, recently is vitalized by a concept that is derived from the motional principle of the Venus flytrap, *Dionaea muscipula*.

1.1 Capabilities and fields of application

The mechanism, which the Venus flytrap, depicted in Figure 1, top left, utilizes to catch its insect prey bases on the controlled manipulation of its cell sap pressure, the turgor, in different layers of depth within the trapping leaf. Thereby the plant makes use of the very efficient, lightweight and accurate fluidic drive system. Huber et al. [1] and Hollerbach et al. [2] compared pneumatic and hydraulic with electromagnetic, polymeric, piezoelectric and other actuators and found advantages regarding specific forces and power. As the Venus flytrap does not consist of separated load bearing and motional cells (cf. Figure 1, top right), there must be a feasible design to integrate both functionalities in one and the same structure. Favorable properties like decrease of weight due to a reduction of components as well as diminished installation space and complexity result.

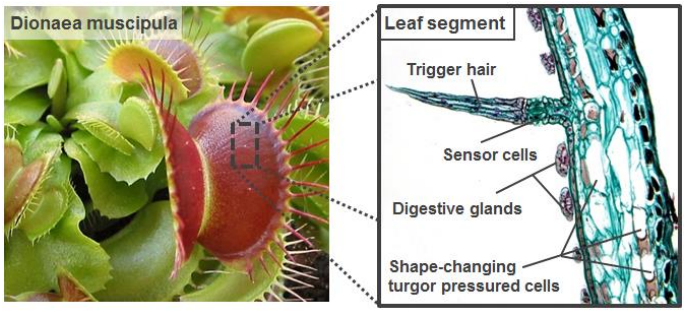

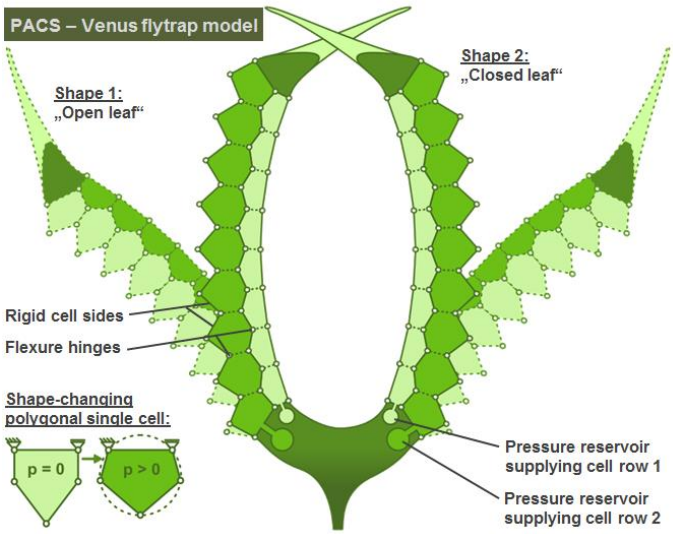

Figure 1: Venus flytrap, *Dionaea muscipula* (top left; photography by J. W. Webb); Microscope slide of Venus flytrap (top right; Copyright Carolina Biological Supply Company); Reproduction of the biological model by PACS (bottom)

Various concepts for adaptive structures are inspired by this working principle. Ranzani et al. [3] developed a medical soft manipulator for minimally invasive surgery. Further soft robot concepts for gripping tools and robotic movement are realized by Ilievski et al. [4] and Guiducci et al. [5]. Zhang et al. [6], [7] theoretically investigate a three-dimensional approach that utilizes closed liquid cell materials for shape-changing structures. Two-dimensional approaches are examined by Lv et al. [8], [9] and Luo Q. et al. [10]. The concept of *Pressure-Actuated Cellular Structures* (PACS) differs from the above morphing structures as it bases on the optimization of discrete cell sides instead of the voids between them. It share most of their advantages with the pressure-adaptive honeycombs (PAH), which are extensively investigated by Vos et al. [11] and Barrett et al. [12] and patented in [13] and [14]. The idea of PACS utilizes the mechanisms of the Venus flytrap for technical use. It provides the possibility to specify arbitrary single-curved structures that deform stepless between predefined states of shape and allow to specifically manipulating its pressure-dependent stiffness. First investigated theoretically by Pagitz et al. [15], a single row PACS demonstrator was subsequently realized by Gramüller et al. [16]. The lower depiction of Figure 1 shows the exemplary imitation of the Venus flytrap with a simplified illustration of a PACS with rigid cell sides and flexible hinges. One arm of this double row structure is realized in the ongoing work of Gramüller et al. [17], which focusses on the sealing of shape-variable polygonal cell tubes.

Automotive applications like spoilers, sunroofs, cladding parts or doors provide advantages regarding actuation efficiency, part reduction and design. Using an already available on-board pressure supply, PACS can provide a lightweight alternative to conventional rigid components. General applications like seats, investigated by Pagitz et al. [18], adaptive hospital beds, shape-variable airfoils for wind power plants and gripping devices can be implemented by utilizing the concept of PACS. Sun shields or photovoltaic systems could be aligned optimally with the sun by PACS, which uses solar radiation to heat and expand fluids within its cells. Aerostatic effects are used for pressurizing PAHs and are investigated by Barrett et al. [12]. Hydrostatic forces in a similar way allow realizing stabilizers for ships.
PACS are conceived to be utilized in an aeronautical application. Rigid aircraft structures restrict available systems in, agility [19], efficiency, operating range [20], [21] and load control [22]. Emission, aerodynamic and functional advantages can be reached by substituting flaps, high-lift systems and spoilers by shape-variable counterparts. A particular promising target structure, the variable-camber wing, is investigated in the following. PACS in this context offer the opportunity to substitute heavy conventional control surfaces, while optimizing the aerodynamic efficiency for multiple flight conditions.

1.2 Objectives

The necessary technology for the implementation of PACS in real-life applications is covered within this article, and extends the theoretical investigations on PACS that are given in [23], [24], and [25]. The transfer of the computationally created truss geometry to a cross sectional geometry, the concept for cell sealing and pressurization as well as manufacturing and assembly issues are the main emphases and part of the herein presented holistic design process. Besides giving the required information about initial and target shape definition, material selection, the specification of load and boundary conditions and form finding, structural characteristics regarding pressure dependent deformation and stresses are discussed in chapter 2. Figure 2 summarizes the necessary sub-steps. The exemplary PACS for realizing a variable-camber wing device is passed through the process chain to demonstrate its functionality. The subsequent *Finite Element Method* (FEM) based simulation (cf. chapter 3) and the experimental investigation of a real-life PACS (cf. chapter 4) evaluate the design process before the results are summarized and open issues for future investigations conclude this work.

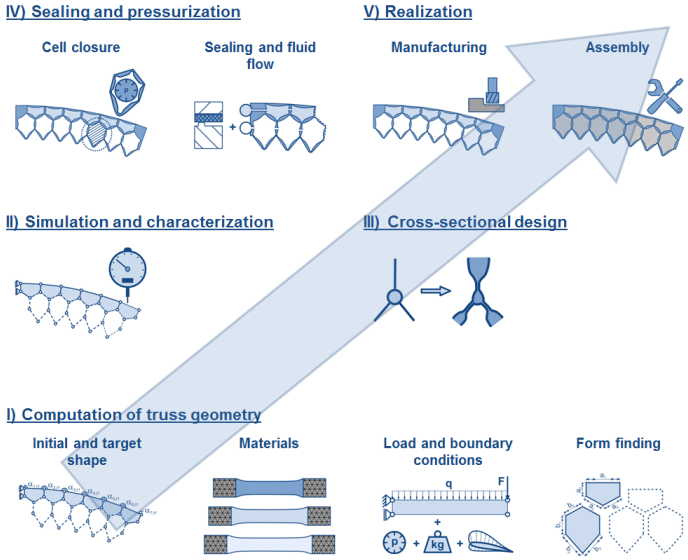

Figure 2: Process steps for the holistic design of PACS

2 Process chain for the holistic design of PACS

On the basis of a two-dimensional truss model, the theoretically deducible potentials for particular applications are examined in the underlying work on PACS and the respective demand for shape-variable structures is clarified. The holistic design process represents the next step to the practicability of this concept. After the computation of the two-dimensional truss geometry, the simulation and characterization allows to compute the required information about the structure's pressure and load dependent behavior. The two-dimensional cross-sectional geometry is subsequently computed, in order

- to meet the underlying truss-model assumptions and
- to control and minimize structural stresses.

Design freedoms granted by the concretization of this abstracted truss model are utilized to reduce structural stresses and to save weight. In the two-dimensional space, fundamental components of a real-life PACS cannot be considered. The axial pressure-tight closure of the cell structure, the design of the fluid flow, the manufacturing and assembly concept intensively affect the overall properties of PACS.
The ability of controlling all of these subcomponents only facilitates the realization of a three-dimensional PACS and permits a high yield of the concept-inherent potential. The required sub-steps for dimensioning a functional PACS (see Figure 2) are determined and explained in detail.

The exemplary structure of a PACS device for realizing the variable camber for a subsonic aircraft wing is passed through the process chain. The generic nature of the introduced process chain shall thus be demonstrated. Thill et al. [26] summarizes the advantages of such an aeronautical technology to

- the improve of aircraft performance for expanding its flight envelope,
- the replacement of conventional control surfaces for flight control to improve performance and stealth,
- the reduction of drag for expanded range and
- the reduction of vibration or for flutter control.

Following the blended wing body configuration of *SAGITTA* [27], a symmetrical profile (here NACA 0012) is chosen for initial configuration. The herein presented PACS is designed to provide a maximum trailing edge deflection of $\Delta\beta = 15°$ and thus achieve a positive camber. The target PACS device is dimensioned to be built of $n_1 = 5$ pentagonal cells in the upper and $n_2 = 6$ hexagonal cells in the lower cell row. The maximum cell pressure of $p = 1.0\ MPa$ is defined for an implementation using glass-fiber reinforced plastic (GFRP) material. Possible arrangements of the PACS within the wing profile can be obtained from Figure 3. The aerodynamic boundary conditions, as well as the resulting changes of the aerodynamic pressure distribution are given in the following subchapters.

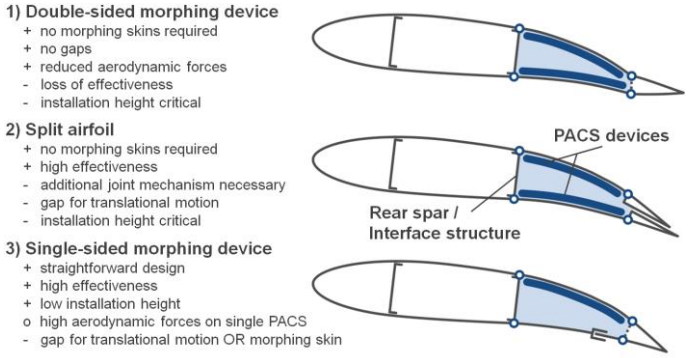

Figure 3: Possibilities for the integration of PACS in a morphing airfoil

2.1 Computation of truss geometry

The initial step for designing PACS is the creation of the two-dimensional truss structure. Therefor two different optimization algorithms have been developed to calculate the shape of each single cell such that the desired behavior is reached. Equal results are achieved by Pagitz et al., who use the approach of volume maximization [23] and the herein utilized approach of virtual work [25] by Gramüller et al.. For the conceptual idea of PACS flexure hinges are used for connecting the rigid cell sides. In contrast to pin joints they provide advantages like fluid tightness and integral manufacturing. The design of the flexure hinges controls the rotational stiffness of the hinge and ultimately the pressure-dependent deformation behavior of PACS. The hinge geometry together with the material properties thus impacts the resulting shape. The process of generating the necessary inputs for the subsequent computations and of the form finding itself is described below. The herein presented investigations do not include the overall computational model following the approach of virtual work, which is needed to numerically calculate PACS. As this work builds on the previously published results, the insights that are given in [25] should be considered.

2.1.1 Initial and target shape

The idea of PACS allows for shape-variable structures that move between specific deformational states. Each cell row h of the PACS thereby opens the possibility to determine an independent target shape at a specific pressure condition. Supplementary the initial state of PACS defines the undeformed and unloaded geometry and thus is of importance for implementations using flexure hinges. The information about the initial geometry is essential for the computation of the hinge stiffness influence and ultimately provides the input for manufacturing. The number of states of shape, which have to be defined is $h + 1$.

For the application of the variable-camber wing, the double-row PACS structure is conceived to move between two target shapes. The target shape is characterized by the shape of the surface cell sides of the first cell row. The respective independent hinge angles are identified in Figure 4. As this structural element of the PACS is conceived only for bending

and not for extensional deformations it is also identified as the neutral fiber of the device. The remaining geometry is not directly affected by the definition of target shapes but is responsible for the pressure-dependent deformation behavior and thus objective of the form finding. The first state to be achieved is given by the NACA 0012 airfoil, between 0.6 and 0.9 of chord length (cf. Figure 8). The second target shape superimposes a circular arc with a deflection of $\Delta\beta = \beta_2 - \beta_1 = 15°$ to the first shape. A lowering at the tip of the airfoil by $15°$ is thus reached.

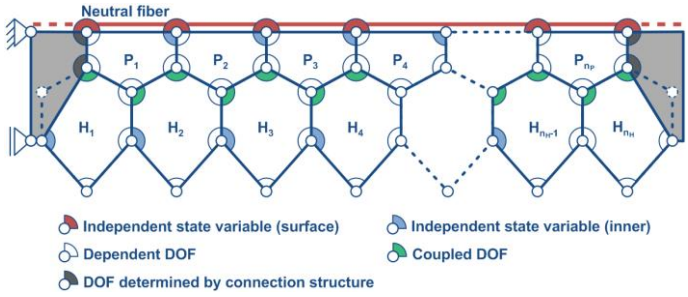

Figure 4: Independent, dependent and coupled degrees of freedom (dof) within a PACS structure

The determination of the initial state yields the potential to lower rotation-based hinge stresses or to satisfy manufacturing needs. For this use case the initial state of shape is defined to be identical with the first target shape. In case of system failure, the remaining stiffness of the PACS provides forces that cause the deformational resetting to the symmetrical NACA profile. In addition to the hinge angles, which are part of the neutral fiber, the remaining, inner, independent state variables have to be determined. Figure 4 illustrates the affected hinge angles.

2.1.2 Materials

The selection of materials, which bases on deformation- and cell-pressure-induced stresses, is illustrated in this section. In contrast to rigid structures or most of the competitive morphing concepts the PACS rely on the cell's pressurization to be able to provide the required stiffness against external forces. These conceptually necessary internal loads lead to prestresses in the structure that have to be borne additionally to external loads. The implementation of flexure hinges as cell side joints results in further bending stresses that concentrate in their extreme fiber and are due to a rotation $\Delta\alpha$. As the hinge element represents the most highly loaded part of the structure, the selection of materials for the application in a PACS is processed to satisfy the demands of these components. The optimal thickness t_{opt}, for a hinge of length s is deduced from a simplified beam model in [16] and can be calculated with

$$t_{opt} = \frac{(R/SF)s}{E|\Delta\alpha|} \quad (1)$$

In order to reduce complexity, these preliminary analytical considerations are deduced for a cell whose edges lie on a circular arc of diameter D. R is the strength, SF the respective safety factor and E the elastic modulus of the considered material. For a given hinge length, deformation, circumcircle with diameter D and $t = t_{opt}$, the material strength limits the maximum tolerable internal pressure to

$$p_{max} = \frac{(R/SF)^2 s}{ED|\Delta\alpha|}. \quad (2)$$

This analytical equation does not consider stress concentrations at thickness transients or due to bending inhomogeneity. As the further design steps allow keeping these effects in tolerable regions, this equation is used for the selection of materials by reference to the target structure. The maximum hinge rotation within the PACS device for the variable-camber wing is calculated to $\Delta\alpha_{VC,max} = 12.54°$ and relates to the first cell of the upper cell row with a size of approximately $D \approx 75\,mm$. The hinge length is defined to $s = 3\,mm$. Table 1 summarizes the suitability of exemplary materials of four classes for this application of PACS. Fatigue-based strength reduction has to be treated within equation (2). For the moment, static datasheet values are used to reduce the pool of potential materials. The preselection of three materials per class allows focusing on the most promising representatives.

Table 1: Material data and resulting optimal thickness and maximum cell pressure at target deformation for variable-camber wing PACS application

Class	*Material*	$E[GPa]$	$R[MPa]$	$t_{opt}[mm]$	$p_{max}[MPa]$
Plastics	PA2200	1.5	50	0.46	**0.30**
	PA12	1.2	50	0.57	**0.38**
	PEEK	3.7	100	0.37	**0.49**
Metals	EN-AW-7075	72	480	0.091	**0.58**
	Ti6Al4V	114	828	0.100	**1.10**
	EN-GJS-1400-1	165	1100	0.091	**1.34**
Elastomers	Elastollan 1160	0.20	50	3.43	**2.28**
	TPU-92A	0.029	19.3	9.12	**2.35**
	Elastollan 1195	0.060	55	12.56	**9.21**
CFRP-fabric	T800+MTM49-3	70	950	0.19	**2.36**
GFRP-UD	HexPly913	42	1200	0.39	**6.27**
CFRP-UD	T800+M21	160	3000	0.26	**10.28**

The presented values, optimal thickness and maximum pressure, are only valid for the specific use case. A reduction of the cell size or an increase of the hinge length would unload the hinges and result in an increase of the optimal hinge thickness. Currently less appropriate materials can thus be taken into consideration. A high ratio of D/s however lowers deviations between real-life PACS and truss model as flexure hinges are approximated with one-dimensional elements.
In addition to the mechanical aspects, two further requirements influence the material selection. Manufacturing issues are discussed in chapter 2.5.1, but can be estimated already with the information about the optimum hinge thickness from Table 1. Pagitz et al. [24] further investigated the influence of the elastic modulus on the accuracy of the form-finding process. They found that the smaller the elastic modulus, the higher the variance between target and resultant shape. Reason for this is the elongation of cell sides, which currently is not considered in the form-finding strategy of Pagitz et al. and in the herein presented work. For $E = 1\,GPa$ a deformational error of about $\eta \approx 40\,\%$ due to this effect is described in the underlying literature for an exemplary geometry. For $E > 20\,GPa$ the error reduces to $\eta < 10\,\%$. The actual form-finding methods for controlling target deformations are accurate for such stiff materials and inadequate regarding elastomers or plastics. Further investigations will allow including the extensional deformation of cell sides and thus improve the accuracy for all groups of materials.
For the subsequent work the GFRP material HexPly913-EC9756 is utilized. Although more appropriate candidates with high elastic modulus are presented, the experience of the authors with this material, regarding material parameters and manufacturing, was decisive (cf. [16]).

2.1.3 Load and boundary conditions

The main purpose for each airborne and ground-based structure and also for PACS is to withstand and bear loads.

Depending on the application conditions different kinds of forces have to be included. After a description of the specific load type, its origin and its preparation for computational use, the integration into the numerical approach for the form-finding process is described.

2.1.3.1 Bearing

Depending on the intended application the bearing conditions have to be defined and integrated in the numerical approach. The utilization of PACS for a variable-camber wing allows conceiving multiple implementations, each with particular boundary conditions. The substitute models presented in Figure 3 show three possible concepts: (1) a double-sided PACS device with closed surface (cf. *Flettner Flap* or servo tab), (2) a split airfoil and (3) a single-sided device with extending surface. The according advantages and disadvantages are listed on the left of the depiction.
In order to reduce complexity and weight and to utilize the load-carrying capabilities of PACS, the single-sided concept is selected for further investigations. The positioning of the active system on the upper side avoids step changes of curvature at the fluid mechanically more sensitive low pressure regions. The bearing is determined to rigidly connect the PACS with the wing's front and rear section and has to transfer forces and momentums.

For the numerical computations, two boundary conditions can be derived from the substitute truss model to eliminate the degrees of freedom (dof), which are constrained by the interface structure. The notation for the structural elements is given according to the underlying work in [25], with the indices for the cell row h, the cell number i and the hinge respectively the cell side j. To constrain the model in the two-dimensional space the positions of two nodes have to be specified. The coordinates $\boldsymbol{X}_{h,i,j} = \boldsymbol{X}_{1,1,9}$ and $\boldsymbol{X}_{1,1,10}$ of the ninth and tenth hinge ($j = 9{,}10$), of the first cell ($i = 1$), in the upper cell row ($h = 1$) are determined to provide translational and rotational bearing. As the rotations of the hinges at both ends of the PACS are disabled by the interface structure, additionally the angles $\alpha_{h,i,j}$ with $[h,i,j] \in [1{,}1{,}9;\ 1{,}1{,}10;\ 1{,}n_1{,}3;\ 1{,}n_1{,}4;\ 2{,}1{,}1;\ 2{,}1{,}2;\ 2{,}1{,}3;\ 2{,}1{,}4;\ 2{,}n_2{,}5;\ 2{,}n_2{,}6;\ 2{,}n_2{,}7;\ 2{,}n_2{,}8]$, have to be kept constant in the numerical computations (cf. Figure 5).

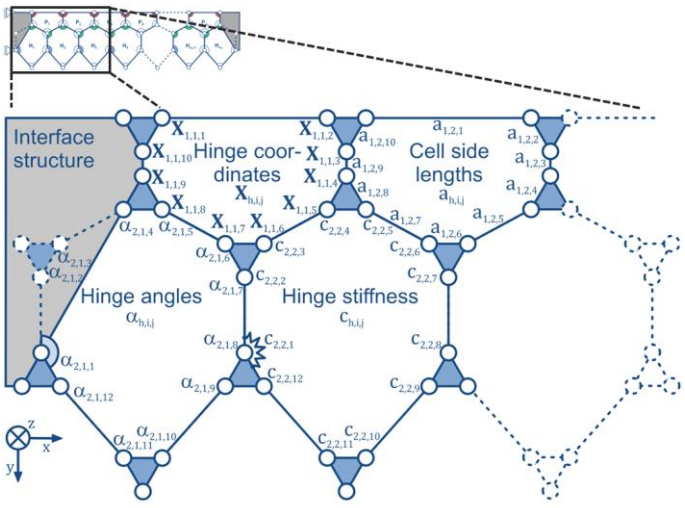

Figure 5: Nomenclature for hinge coordinates, cell side lengths, hinge angles and hinge stiffness

The bearing of the PACS device within the airfoil allows applying internal and external forces.

2.1.3.2 Flexure hinges

For the accurate dimensioning of compliant PACS the consideration of the flexure hinge stiffness is inevitable. A PACS of infinitesimal hinge stiffness would reach its equilibrium state already at an infinitesimal cell pressure. The characteristic pressure-dependent deformation, transition and stiffening phases [16] that are investigated extensively in chapter 2.2, show the influence of rotational hinge stiffness on the computational outcomes. Assuming constant bending over the hinge lengths, the elastic modulus of the applied material E, the second moment of inertia in plane-perpendicular direction $I_{z,\boldsymbol{k}}$ and the hinge length $s_{\boldsymbol{k}}$ at hinge $\boldsymbol{k} = [h,i,j]$ provide the necessary input for the flexure hinge with rectangular cross section. In similarity with the approach that is used by Pagitz et al. [23], the hinges are modelled as beams. For a non-varying thickness $t_{\boldsymbol{k}}$ along the flexure hinge, the stiffness $c_{\boldsymbol{k}}$ at hinge $\boldsymbol{k}$ can be calculated by

(3) $c_{\boldsymbol{k}} = \frac{EI_{z,\boldsymbol{k}}}{s_{\boldsymbol{k}}} = \frac{Et_{\boldsymbol{k}}^3 d}{12 s_{\boldsymbol{k}}}$.

For the two-dimensional model, the depth $d = 1\,m$ is used in the following. The hinge stiffness is considered in the numerical model by the force vector $\boldsymbol{f}_c$, which depends on the rotation $u_{\boldsymbol{k}}$:

(4) $\boldsymbol{f}_c = -\boldsymbol{c}\Delta\boldsymbol{\alpha}$.

The computation of the energy potential $\dot{\Pi}$ is used to calculate the equilibrium state. For the vanishing global potential $\dot{\Pi} = 0$ the vector of independent state variables and optimization vector $\boldsymbol{u}$ states the structural equilibrium. The hinge momentums are considered by

(5) $\dot{\Pi}_{c,\boldsymbol{k}} = -\frac{\partial W_{c,\boldsymbol{k}}}{\partial u_{\boldsymbol{k}}} = -\frac{\Sigma_{\boldsymbol{k}} f_{c,\boldsymbol{k}} \delta u_{\boldsymbol{k}}}{\delta u_{\boldsymbol{k}}}$.

As it can be obtained from equation (4) the hinge momentum $\boldsymbol{f}_c$ counteracts any deformations from the manufacturing state of the structure and is thus negative in the local rotational coordinate system. The subsequently presented forces are responsible for these deformations.

2.1.3.3 Internal pressure

As its operating principle bases on the pressurization of polygonal cells, the first and inevitable load type for PACS is predefined by the internal fluidic pressure. Pressure loads acting on cell sides represent the driving force for deformations and further cause the overall structural stiffness. For calculating the truss geometry of the target PACS the internal cell pressure p_{int} is a necessary input and thus considered as known. For the cell side lengths $\boldsymbol{a}$, the resulting vector of pressure forces is

(6) $\boldsymbol{f}_p = p_{int}\boldsymbol{a}d$.

The energy potential can be computed as the derivative of virtual work $\partial W_{\boldsymbol{k}}$ at a change of the rotational dof $u_{\boldsymbol{k}}$, to

(7) $\dot{\Pi}_{p,\boldsymbol{k}} = -\frac{\partial W_{p,\boldsymbol{k}}}{\partial u_{\boldsymbol{k}}} = -\frac{\Sigma_{\boldsymbol{k}} f_{p,\boldsymbol{k}} \delta r_{p,\boldsymbol{k}}}{\delta u_{\boldsymbol{k}}}$.

$\delta r_{p,\boldsymbol{k}}$ is the cell side-perpendicular displacement at the cell side $\boldsymbol{k}$, due to the virtual displacement $\delta u_{\boldsymbol{k}}$. The pressure on each cell side is thus evaluated in the numerical computation.

2.1.3.4 Inertial forces

Depending on the acceleration of the structure, the mass of PACS influences its pressure-dependent behavior. The inertial forces can be calculated with knowledge of the applied

material's density ρ and the cross-sectional area $A_{\boldsymbol{k}}$ of cell side $\boldsymbol{k}$ to

(8) $\boldsymbol{f}_g = \rho \boldsymbol{A} d\ddot{x} \begin{bmatrix} \cos(\theta) \\ \sin(\theta) \end{bmatrix}$

for the acceleration $\ddot{x}$ and its angular orientation θ in the xy-plane. Density and acceleration can be identified before the form-finding process. The cross-sectional area of the PACS in contrast depends on the individual cell side lengths and thickness distribution which are determined in the form-finding process and the cross-sectional design. As the inertial forces in turn affect the resulting truss geometry, an iterative process is implemented to approach the target state of shape. The energy potential is calculated with the inertial force-parallel component of the virtual displacement $\delta r_{g,\boldsymbol{k}}$, such that

(9) $\dot{\Pi}_{g,\boldsymbol{k}} = -\frac{\partial W_{g,\boldsymbol{k}}}{\partial u_{\boldsymbol{k}}} = -\frac{\sum_{\boldsymbol{k}} f_{g,\boldsymbol{k}} \delta r_{g,\boldsymbol{k}}}{\delta u_{\boldsymbol{k}}}$.

The effects of the herein considered gravitational forces can be observed best at low cell pressures. As the stiffness of a given structure is reduced for decreasing pressures, the impact of inertial forces on the deformation is increasing. As the influence of weight simultaneously increases for high accelerations and materials of great density, it cannot be neglected. A profound dimensioning of PACS hence includes these forces.

The mass of a PACS depends on its cross-sectional design and cannot be extracted from the herein used truss model. The transfer between truss model and two-dimensional model is done in a subsequent process that is described in chapter 2.3. The change of structural masses and according inertial forces is calculated in an iterative process to provide relief. The initial overall mass of $m_0 = \rho A d = 10.0e-3\ t$ results from the initially assumed cross-sectional area of $A_0 = 5.56e3\ mm^2$, the density of HexPly913-EC9756 of $\rho_{HexPly913} = 1.80e\text{-}9\ \frac{t}{mm^3}$ and a depth of one meter. Figure 6 shows the iterative process, which is utilized to update the cross-sectional area (CSA) and related structural mass according to the actual shape.

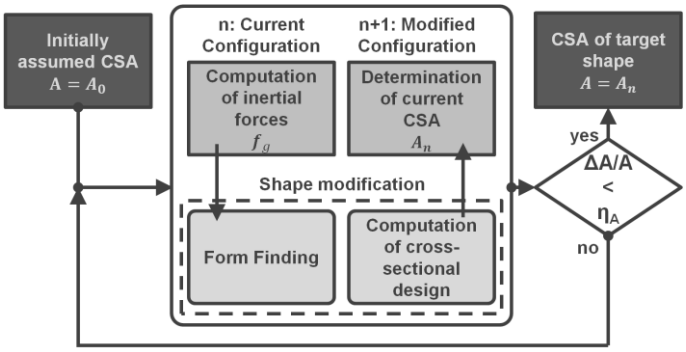

Figure 6: Flow chart for the iterative computation of the structure's CSA

The change of the structural mass $\Delta m = \rho d \Delta A$ is depicted in Figure 7 for the given variable-camber wing example. A negligible change of the cross-sectional area η_A, and thus of the structural mass ($\Delta m/m < 1e-4$), results after two iterations.

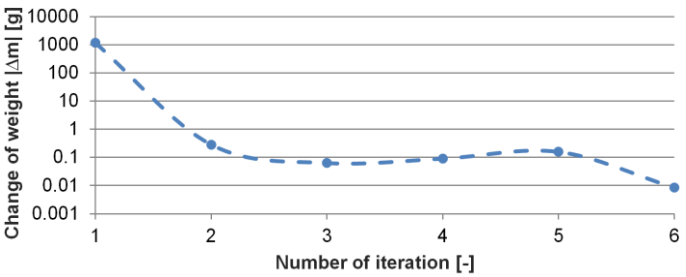

Figure 7: Change of weight during iterations of form-finding

2.1.3.5 Point loads

As it can be obtained from Figure 3 the single-sided concept for the variable-camber wing leads to additional forces and momentums at the non-supported side of the PACS. The lower aerodynamic skin is conceived to allow extensional deformations and simultaneously to prevent from bending. Linear bearings or shear-flexible morphing skins [28] can be used to realize the necessary mechanism. Besides the subsequently introduced aerodynamic forces, which act on the PACS surface, external bearing forces result from the rigid end section. Surface-perpendicular pressure loads at the tip and lower skin of the aerodynamic profile are supported by the PACS and have to be considered.

Shown for the example of this specific application, the necessity for the implementation of point loads in the form-finding process is manifold. A modular PACS structure generally is connected at both of its ends to allow for the transfer of loads. The application of loads across the connecting structure is intended. Point loads can be applied to the model at hinge points $\boldsymbol{f}_{pl,\boldsymbol{k}}$ or at additional external points $\boldsymbol{f}_{pl,ext,o}$ which can be connected rigidly to two hinge points. The related force vector is

(10) $\boldsymbol{f}_{pl} = [\boldsymbol{f}_{pl,\boldsymbol{k}} \quad \boldsymbol{f}_{pl,ext,o}]$.

The energy potential is calculated with the force-parallel virtual displacement $\delta r_{pl,\boldsymbol{k}}$, respectively $\delta r_{pl,ext,o}$ resulting from $\delta u_{\boldsymbol{k}}$, to

(11) $\dot{\Pi}_{pl,\boldsymbol{k}} = -\frac{\partial W_{pl,\boldsymbol{k}}}{\partial u_{\boldsymbol{k}}} = -\left(\frac{\sum_{\boldsymbol{k}} f_{pl,\boldsymbol{k}} \delta r_{pl,\boldsymbol{k}}}{\delta u_{\boldsymbol{k}}} + \frac{\sum_{\boldsymbol{k}} f_{pl,ext,o} \delta r_{pl,ext,o}}{\delta u_{\boldsymbol{k}}}\right)$.

2.1.3.6 Aerodynamic forces

With the advantages of aerodynamic efficiency, weight saving and flight performance enhancements, the implementation of the aeronautical PACS structure is to be conceived. In [15], it is shown that the truss geometry of PACS can be calculated such that predefined shape functions can be reached for different pressure settings. Though they have critical influence on the resulting deformations, the underlying work on PACS does not include external forces in the form-finding process. Consequently, the aerodynamic characteristic of such an active camber wing is not adequately controllable with presence of operational loads. As the resulting aerodynamic forces on the wing profile depend on its actual shape, the effects of the negligence of these loads in the form-finding process additionally cannot be computed without iterations for the consideration of aeroelasticity. In the following, the approach presented in [25] is thus extended for the consideration of external aerodynamic loads.

The integration of the PACS is conceived to substitute the conventional wing from 0.6 to 0.9 of the chord length. A deflection angle of $\beta_2 = 15°$ shall be reached at the tip of the profile, based on the initial NACA 0012 geometry. For the results presented in the following, the chord length c_{CL}, the flight velocity v_∞, the ambient temperature T_∞ and pressure p_∞ and the kinematic viscosity ν are given in Figure 8. It can be seen that the moderate deflection of 15°, what means 3° per cell in the first cell row, is sufficient for an increase of lift by the factor 2.52 to $L = 4.55\ kN$ per meter wing span. For the assumed Reynolds number of $Re = 7.38$ an increase of the lift-to-drag ratio from $C_L/C_D = 69.50$ to $C_L/C_D = 117.48$ results for the varied airfoil shape.

For the realization of a gapless trailing edge flap, the panel method-based software XFOIL is used to compute the two-dimensional aerodynamic pressure distribution on the unmodified and deformed NACA 0012 profile. The results from the aerodynamic computations are visualized in Figure 8.

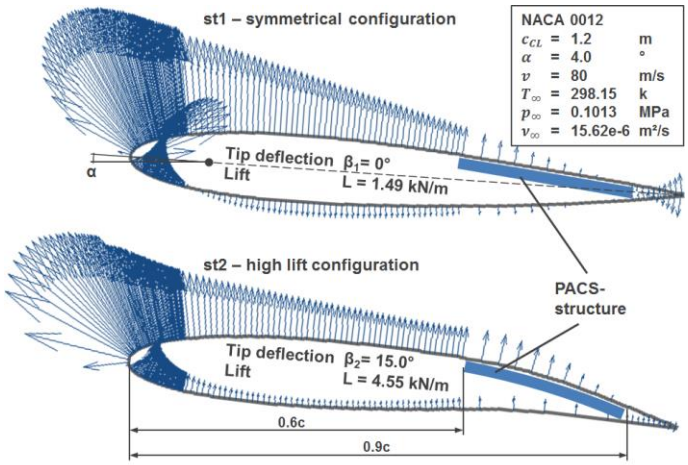

Figure 8: Utilization of PACS for realizing the variable chamber wing and resulting aerodynamic forces

Similar to the internal pressure, the aerodynamic pressure load is applied to the surface cell sides of the upper cell row. The related force vector and energy potential are given with

(12) $\boldsymbol{f}_{ad} = p_{ad}\boldsymbol{a}d$ and

(13) $\dot{\Pi}_{ad,\boldsymbol{k}} = -\frac{\partial W_{ad,\boldsymbol{k}}}{\partial u_{\boldsymbol{k}}} = -\frac{\Sigma_{\boldsymbol{k}} f_{ad,\boldsymbol{k}} \delta r_{ad,\boldsymbol{k}}}{\delta u_{\boldsymbol{k}}}$.

The computation of the essential forces that act on the PACS and their integration in the process of form finding, allows designing a shape-variable structure that moves between predefined form functions in presence of internal and external forces.

2.1.3.7 Example: *Beam pendulum*

At the example of a beam pendulum, a simple mechanical problem shall be used to describe the inclusion of the discussed loads in the computational model respectively the approach of virtual work. The first depiction of Figure 9-(a) shows the beam pendulum with a hinged bearing (1), a rotational spring (2), which represents the stiffness of a flexure hinge c, and the internal pressure load p (3). It is assumed that the rotational spring is without preloads at $\alpha_B = 0°$.

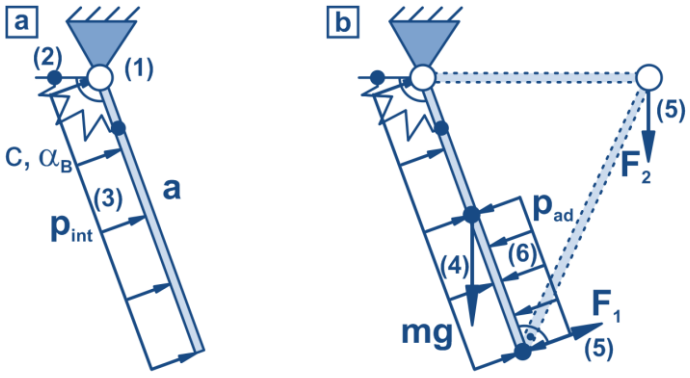

Figure 9: Beam pendulum model for the declaration of the method of virtual work; a) basic model; b) extended modeling variant

Similar to the computation of the PACS truss geometry, the equilibrium state shall be reached at a specific hinge angle α_B that corresponds to $u_{\boldsymbol{k}}$ by determination of the beam length a for the depth d. The virtual work and the energy potential for this kinematic system is given by

(14) $\delta W = \underbrace{-c\left(\alpha_B \delta\alpha_B + \frac{1}{2}\delta\alpha_B^{\,2}\right)}_{(2)} + \underbrace{\frac{1}{2}p_{int}a^2 d\delta\alpha_B}_{(3)}$

(15) $\dot{\Pi} = -\frac{\delta W}{\delta\alpha_B} = c\left(\alpha_B + \frac{1}{2}\underbrace{\delta\alpha_B}_{\approx 0}\right) - \frac{1}{2}p_{int}a^2 d = 0.$

As presented in [25], the system of equations for a complete PACS structure is to be computed numerically. For the example of the beam pendulum an analytical solution can be derived. The resulting beam length is

(16) $a = \sqrt{\frac{2c\alpha_B}{p_{int}d}} = \sqrt{\frac{Et_k^3\alpha_B}{6s_k p_{int}}}$.

As it can be seen, for a beam pendulum with a flexure hinge of stiffness c, the equilibrium state is independent from the depth d. In order to complete the mechanical model for the consideration of inertial forces (4), point loads (5) and external pressure loads (6) the beam pendulum example is extended in Figure 9-(b). The virtual work is

(17) $\delta W = \underbrace{-c(\alpha_B\delta\alpha_B + \frac{1}{2}\delta\alpha_B^2)}_{(2)} + \underbrace{\frac{1}{2}(p_{int} - \frac{3}{4}p_{ad})a^2 d\delta\alpha_B}_{(3+6)} + \underbrace{\frac{1}{2}mgsin(\alpha_B)a\delta\alpha_B}_{(4)} + \underbrace{(F_1 - \frac{3}{2}F_2)a\delta\alpha_B}_{(5)}.$

The necessary beam length for adjusting the equilibrium state at the angle α_B results from

(18) $\dot{\Pi} = \left[\frac{1}{2}p_{int} - \frac{3}{8}p_{ad}\right]a^2 d + \left[\frac{1}{2}mgsin(\alpha_B) + F_1 - \frac{3}{2}F_2\right]a - c\alpha_B$

The implementation of load and boundary conditions is described and specified at the example of a beam pendulum. The necessary input for dimensioning the variable-camber wing in the form-finding process is completed.

2.1.4 Form finding

The computation of the PACS geometry is done in the form-finding process. The determination of initial and target state and of materials for hinges and cell sides, together with loads and bearing conditions provide the necessary input for the form-finding. For the herein presented form-finding process the underlying work of Gramüller et al. [25] is extended to suit the specific use case. Figure 10 visualizes the implemented information before the first iteration step is processed. Each cell side of the neutral fiber is calculated to have a length of $a = 72.4\,mm$. Thus it is suited to the aerodynamic profile between 0.6 and 0.9 of the chord length. Depending on these known cell side dimensions, which are not altered during form finding, the unknown cell side lengths, or optimization variables, are applied with an initial length (cf. Figure 10). The rigid elements at both ends of the PACS are used to mechanically connect the shape-variable structure to the airfoil. Based on the manufacturing state of shape, the material selection and hinge geometry, a first computation of stresses, due to hinge rotation can be processed. As the first target shape (st1) is identical with the initial state, the rotation induced stresses vanish. For the second target shape (st2), the maximum hinge rotation $\Delta\alpha_{st2,max} = 7.34°$ can be extracted. For $t = 0.22\,mm$ the maximum stress of

(19) $\sigma_{st2,init,max,rot} = \frac{Et_k}{2s_k}|\Delta\alpha_{\boldsymbol{k}}| = 197.29\,MPa$ results.

Stresses in hinge and cell side elements are visualized according to the depicted legend. Aerodynamic, point loads and inertial forces are shown relatively to each other and with their

orientation. The internal pressure in each cell row forms the driving forces for deformation, and is chosen to $\boldsymbol{p}_{int,st1} = [0.1, 1.0]$ for the first and to $\boldsymbol{p}_{int,st2} = [1.0, 0.1]$ for the second target state of shape.

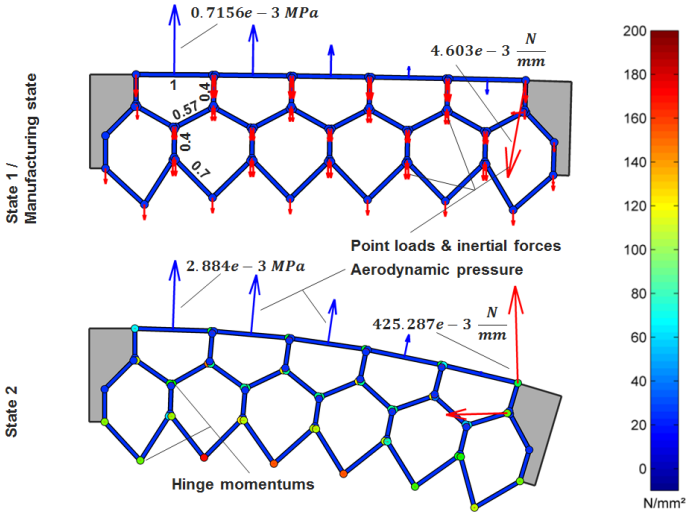

Figure 10: Initial configuration for form-finding process in variable-camber wing application and deformation-based stresses

In contrary to the beam pendulum example, the system of equations for a PACS with multiple cells and cell rows is extensive and thus solved numerically. With knowledge of the partial energy potentials, the equilibrium state of the structure is found by evaluating equation (20).

$$(20)\ \dot{\Pi} = \dot{\Pi}_c + \dot{\Pi}_p + \dot{\Pi}_g + \dot{\Pi}_{pl} + \dot{\Pi}_{ad} = 0$$

The optimization variables are given by all cell side lengths and hinge angles, except for those describing the neutral fiber. A more detailed insight in the underlying form-finding strategy is presented in [25]. The resulting truss structure for the use case of the variable-camber wing is depicted in Figure 11. The concentration of rotation-based and normal stresses in the thin-walled hinge elements leads to

$$(21)\ \sigma_{st1,max} = \frac{Et_k}{2s_k}|\Delta\alpha_k| + \underbrace{\frac{\partial W_k}{\partial a_k}\frac{1}{t_k d}}_{\approx \frac{pr}{t_k}} = 536.17\ MPa,$$

at hinge $\boldsymbol{k} = [1,1,4]$ for $st1$. The utilization of material strength is thus 44.7 % in the most highly stressed hinge (see enlarged section).

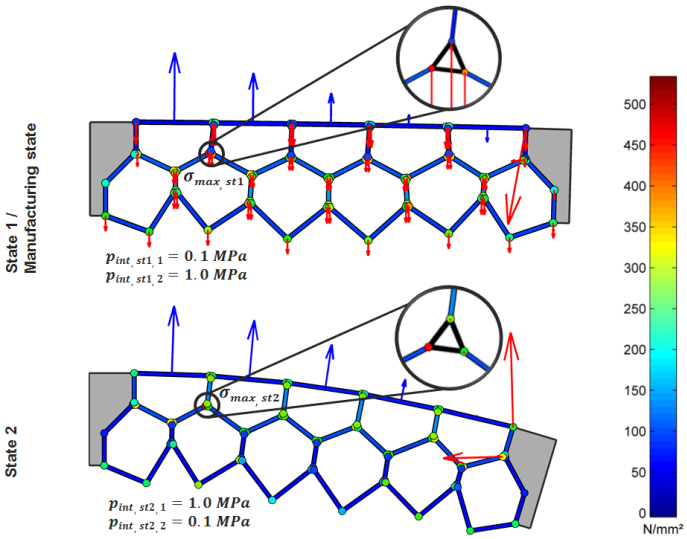

Figure 11: Resulting truss geometry and structural stresses after form finding of PACS, in variable-camber wing application

Local stress concentrations due to transitions of wall thickness between hinge and cell side elements are not considered. The subsequent computations, based on FEM shall be used for detailed stress analysis. With the calculation of cell side lengths the first step of the holistic design of PACS, the computation of the truss geometry is completed.

2.2 Simulation and characterization

With dimensioning the PACS according to the described computation of truss geometry, three isolated states of shape are known, together with the according structural loads. The deformational reaction on changing external forces at these states and in general, or in other words the stiffness of the structure, is as unfamiliar as the effects of changing cell pressures. For the use case of the variable-camber wing this means that the deformation and thereby the aerodynamic characteristics of the wing are only known for three specific pressure and load states. A change in flight velocity, angle of attack or cell pressure leads to an unknown wing shape. The structural behavior of a PACS in dependence on forces and internal pressures is thus investigated in this section.

As described and experimentally validated for a single cell in [16] the pressure-dependent deformation of PACS can be divided in three phases, *deformation* (I), *transition* (II) and *stiffening* (III). An equal behavior is observed for the cell compound. As it is shown in Figure 12 for the given use case, these deformation phases can be found both for single pressurized cell rows and for a constant ratio of pressure between different cell rows. The rotation $\Delta\beta$ corresponds to the orientation of the upper cell side ($i = 1$) of the last cell in the first cell row (labelled in Figure 12). It depends on the behavior of all intermediate cells between this cell and the bearing and thus provides a cumulative deformation value. It is posed for different pressure factors *f*, which are multiplied with three varying pressure sets, given in the legend.
Depending on the ratio of cell row pressures, it is shown that the rotational angle $\Delta\beta$ can be adjusted between $-1.0°$ and $28.7°$ for non-existent external forces. Besides the investigation of the deformational performance of the PACS, the stiffness and strength properties are examined. Figure 13 depicts the rotational deformation together with the maximum stresses σ_{max} for the pressure sets that are defined for target shape *st1* and *st2*. Five main conclusions can be deduced.

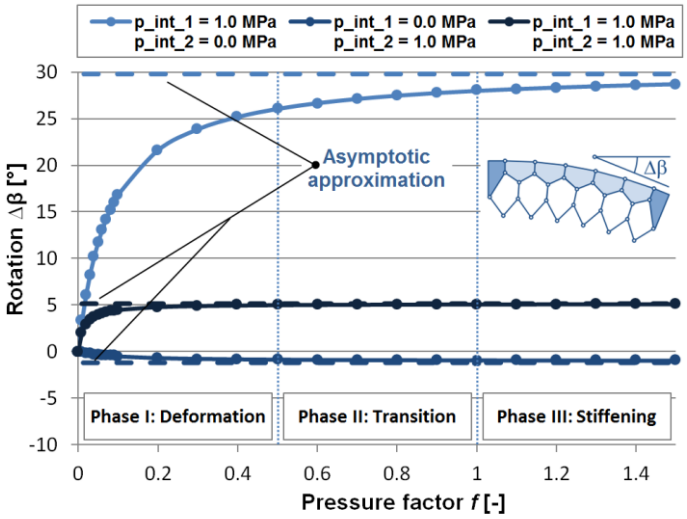

Figure 12: Pressure dependent deformation and stiffening behavior for separated and combined pressurization

First, a PACS structure loaded with external forces may collapse for low internal pressures. An increase of hinge stiffness and cell pressure prevent from excessive deformations. For the given structure, the black double line in Figure 13 marks the minimum pressure factor assuming the load set of the respective target state of shape.
Second, the structural stresses do not imperatively rise with increasing external forces. Depending on their orientation with respect to the actual deformations, external forces may also reduce the maximum total stress of a PACS by counteracting local deformation and bending.
Third, the achievement of the asymptotic deformation for a finite pressure factor (cf. Figure 12 and Figure 13) is delayed by increasing external forces and hinge stiffness.

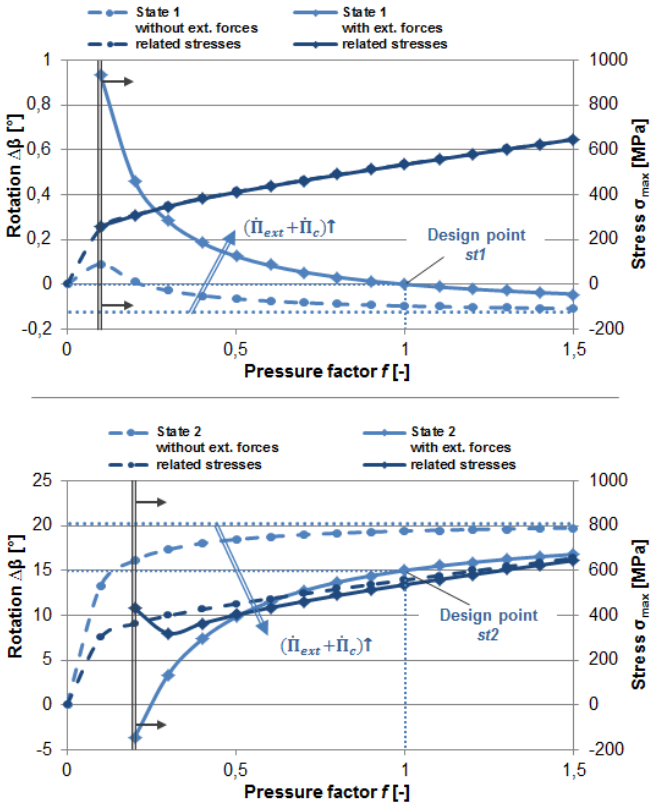

Figure 13: Pressure dependent deformation and structural stresses for design pressure setting, with and without related external forces from variable-camber wing application

Fourth, the greater the distance between target state of shape and asymptote, the greater is the impact on this state of shape from a deviation of the cell pressure factor.
Fifth, the stiffness against external forces is different for each pressure ratio. The effects of external loads on the structural deformation have to be computed for each relevant load case.

Beside the control of shapes, the possibility of influencing structural stiffness provides additional opportunities. The symmetrical wing profile configuration is adjusted for the pressure ratio $\boldsymbol{p}_{int,st1}$. In this case, the second cell row is pressured more intensively than the first one. Due to the cells distance to the neutral fiber and thus the longer lever arm, the stiffness of the PACS at shape $st1$ exceeds the one of $st2$, which is mainly defined by pressure forces on the first cell row. An increase of airfoil stiffness prevents from flutter and unfavorable dynamic lift effects. The stiffer state of shape was thus chosen to form the symmetrical airfoil, which is conceived as cruising, or high speed configuration. Barrett et al. [12] moreover describes the advantageous effects of flexible flaps on the flight safety in case of microbursts during take-off and landing. Thereby, a decreased stiffness for the high lift configuration is preferential as it lowers lift peaks, which result from a changing air speed.

2.3 Cross-sectional design of cell compound

The computation of truss geometry reduces the PACS to a truss model for saving calculation time and to diminish initial design efforts. This section describes the creation of the cross-sectional design, which matches the reduced truss model. The assumptions that are made in the previous design steps have to be considered. Rigid cell sides, eccentric nodal hinges with constant spring stiffness and rigid connection structures at both ends of the PACS are approached in the following subchapters. The according notation and the results from dimensioning the PACS for the variable-camber wing are illustrated in Figure 14.

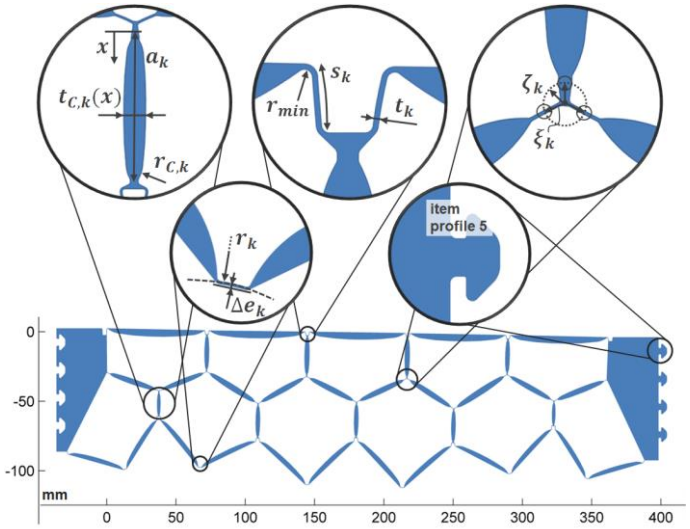

Figure 14: Resulting cross section for the variable-camber wing PACS device and respective design parameters

With the design of the cross-sectional area of PACS, the three-dimensional cell body can be formed by extrusion. In this regard, the areal dimensioning completes the draft design for the realization of PACS.

2.3.1 Cell sides

For the dimensioning of cell sides the main objectives are to approach the assumption of rigidity and to fulfill the demand for

structural strength regarding the selected material. The axial stiffness of a rectangular beam with elastic modulus E, cross-sectional area A and varying thickness $t_{C,\boldsymbol{k}}(x)$ is

(22) $c_{a,\boldsymbol{k}} = \frac{EA_{\boldsymbol{k}}}{a_{\boldsymbol{k}}} = \frac{Ed\int_0^{a_{\boldsymbol{k}}} t_{C,\boldsymbol{k}}(x)dx}{a_{\boldsymbol{k}}^2}$.

The according axial stress due to an axial cell side force $f_{a,\boldsymbol{k}}$ is

(23) $\sigma_{a,\boldsymbol{k}} = \frac{f_{a,\boldsymbol{k}}}{A_{\boldsymbol{k}}} = \frac{f_{a,\boldsymbol{k}}}{dt_{C,\boldsymbol{k}}(x)}$.

Additionally, these truss elements are loaded with cell-side-perpendicular pressure loads, which cause bending. The bending stiffness $c_{b,\boldsymbol{k}}$ can be calculated based on equation (3), to

(24) $c_{b,\boldsymbol{k}} = \frac{EI_{z,\boldsymbol{k}}}{s_{\boldsymbol{k}}}$, with

(25) $I_{z,\boldsymbol{k}} = \int_0^{t/2} t_{C,\boldsymbol{k}}^2(x)dxdz = \frac{dt_{C,\boldsymbol{k}}^3(x)}{12}$.

The bending stresses at the extreme fiber of a beam can be calculated by evaluating

(26) $\sigma_{b,\boldsymbol{k}} = \frac{M_{C,\boldsymbol{k}}(x)t_{C,\boldsymbol{k}}(x)}{2I_{z,\boldsymbol{k}}}$, with

(27) $M_{C,\boldsymbol{k}}(x) = \frac{1}{2}[-p_{\boldsymbol{k}}dx^2 + (pda_{\boldsymbol{k}} + 2f_{l,\boldsymbol{k}})x + 2M_{C,\boldsymbol{k}}]$.

The momentum $M_{C,\boldsymbol{k}}(x)$ at cell side $\boldsymbol{k}$ results from the local wall pressure, lateral cell side forces $f_{l,\boldsymbol{k}}$ and the hinge momentum M_k at an equilibrium state of shape. Both values are available from the prior executed simulation. The cell side stresses depending on the position x of the cell side result from the superposition of axial and bending stresses:

(28) $\sigma_{tot,\boldsymbol{k}} = \sigma_{a,\boldsymbol{k}} + \sigma_{b,\boldsymbol{k}} = \left|\frac{f_{a,\boldsymbol{k}}}{dt_{C,\boldsymbol{k}}(x)}\right| + \left|\frac{3[-p_{\boldsymbol{k}}dx^2+(pda_{\boldsymbol{k}}+2f_{l,\boldsymbol{k}})x+2M_{\boldsymbol{k}}]}{dt_{C,\boldsymbol{k}}^2(x)}\right| \stackrel{!}{=} \frac{R}{SF_{CS}}$.

The minimum wall thickness for cell side at position x due to stress limitations is thus

(29) $t_{C,\boldsymbol{k},min}(x) = \frac{f_{a,\boldsymbol{k}}+\sqrt{f_{a,\boldsymbol{k}}^2+24Rd/SF_{CS}|M_{C,\boldsymbol{k}}(x)|}}{2Rd/SF_{CS}}$.

For the PACS structure depicted in Figure 14, this stress criterion was used to dimension the cell side thicknesses. As mentioned in chapter 2.1.2, the stiffness of the cell sides impacts the accuracy of the translation from the reduced truss model to the resulting 2D geometry. According to the equations (22), (24) and (25), a raise of wall thickness increases axial stiffness linearly and bending stiffness with the third power. For consideration of stiffness issues a safety factor for cell sides of $SF_{CS} = 8$ is thus chosen for the underlying use case.
The load state is changing for varying pressures, deformation states and external forces. The herein presented methods allow designing the PACS cross sectional area for one load state. A superposition of cell side thicknesses, which result from all design driving load states, would lead to the compliance of the safety factor for each load condition.

2.3.2 Flexure hinges

In the truss model hinges are assumed to be concentrated to a single point and possess a constant rotational stiffness. The resulting demands on a real flexure hinge of finite length with specific orientation and curvature are discussed subsequently.

The determination of hinge length and thickness is part of the computation of truss geometry, as it results in the stiffness and thus influences the deformation characteristic. The optimum thickness is calculated according to equation (1).
To prevent additional stresses and deformations due to lateral forces, the flexure hinges are aligned parallel to the direction of the resultant force. The information of hinge forces can be evaluated at the truss model. The orientation vector $\xi_{\boldsymbol{k}}$ at the hinge intersection with radius $\zeta_{\boldsymbol{k}}$ is thus defined to minimize stresses for a specific load state (see Figure 14).
Equally to the hinge direction, the curvature of the hinge is designed on the basis of the actual loads. Besides the eliminated lateral bearing forces, the dimensioning of the hinge thickness according to equation (1) does also not include bending stresses due to normal bearing forces and improper curvature. The target curvature $\kappa_{DP,\boldsymbol{k}}$ at the design point DP of an optimal aligned flexure hinge of length $s_{\boldsymbol{k}}$ under a pressure load p_k and resultant force $f_{tot,\boldsymbol{k}}$ is given by

(30) $\kappa_{DP,\boldsymbol{k}} = \frac{1}{r_{\boldsymbol{k}}} = \frac{dt_{\boldsymbol{k}}p_{\boldsymbol{k}}}{f_{tot,\boldsymbol{k}}t_{\boldsymbol{k}}} = \frac{dp_{\boldsymbol{k}}}{\sqrt{f_{a,\boldsymbol{k}}^2+f_{l,\boldsymbol{k}}^2}}$, deduced from

(31) $r = \frac{\sigma t}{p}$ (pipe formula)

The hinge direction and curvature are both calculated for the deformed state of the PACS. The change of orientation and the hinge deformation between initial and design state have to be considered. As the hinge $\boldsymbol{k}$ is rigidly connected to its cell side $\boldsymbol{k}$, its hinge orientation can be calculated for the manufacturing state by subtracting the respective cell side rotation. The manufacturing curvature is thus adjusted in order to consider the local hinge rotation $\Delta\alpha_{\boldsymbol{k}}$:

(32) $\kappa_{st0,\boldsymbol{k}} = \kappa_{DP,\boldsymbol{k}} - \frac{\Delta\alpha_{\boldsymbol{k}}}{s_{\boldsymbol{k}}}$.

In contrary to the dimensioning of cell sides, the hinge geometry is dimensioned for one specific design point. For the underlying use case this load state is determined to be $p_{int,DP,1} = p_{int,DP,2} = 1.0MPa$, which means maximum pressure load applied to both cell rows. External forces are neglected in this example, as their influence on structural stresses decreases for increasing pressures. It should be noticed that for load states, varying from the design point, the hinge geometry is not optimal. The design point has thus to be chosen to cause the maximum stresses in the PACS. As prospect to further investigations, the consideration of multiple design points in this context will improve the two-dimensional design.
For a straight flexure hinge of finite length $s_{\boldsymbol{k}}$ the concentrated or effective hinge position can be assumed to be located at the center of the hinge line. The length reduction due to deformation-induced curvature is neglected by this assumption. As the hinges are not designed to be straight in their manufacturing state, the effective hinge position doesn't lie on the hinge line. The distance between hinge chord midpoint and necessary effective hinge (see Figure 15) shall be considered in the design point by integrating over the distributed hinge.

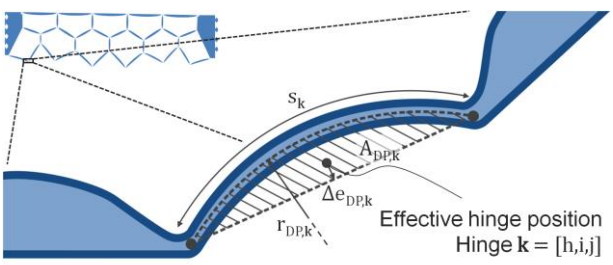

Figure 15: Distance between hinge chord and effective position of flexure hinge

The distance of the effective hinge point from the hinge's chord line $\Delta e_{DP,k}$ is calculated by integrating the distance between hinge and chord line $e_k(s)$ over the hinge length s_k:

$$(33)\ \Delta e_{DP,k} = \frac{1}{s_k}\int e_k(s)ds_k = \frac{2r_{DP,k}^2}{s_k}\left(\sin\left(\frac{s_k}{2r_{DP,k}}\right) - \frac{s_k}{2r_{DP,k}}\cos\left(\frac{s_k}{2r_{DP,k}}\right)\right).$$

The accurate position of the hinge is essential for the deformational characteristic of the PACS. For arbitrary hinge rotation $\Delta\alpha_k$ the distance $\Delta e_{DP,k}$ of the hinge chord to the effective hinge position has to be adjusted in the manufacturing state indifferent to the initial offset $\Delta e_{st0,k}$.
The advances in terms of structural stresses due to the force and deformation-based two-dimensional design are confirmed in the subsequent evaluation (see chapter 3). The therein presented values show that the maximum stresses for an off-design pressure ratio exceed the stresses in the design point significantly. A decrease of the equivalent stress from $\sigma_{vM,max,I} = 2541.61\,\text{MPa}$ and $\sigma_{vM,max,II} = 2525.10\,\text{MPa}$ to $\sigma_{vM,max,III} = \sigma_{vM,max,DP} = 901.01\,\text{MPa}$, for the design point, is examined for a pressure factor of 1 by FEM-based computations. For the observed load cases the maximum stresses are reduced to the percentage of 35 %. The advantages regarding stress reduction of a load-based cross-sectional PACS design are thus shown.

2.3.3 Connection structure

The connection of PACS to a conventional structure or to other PACS segments in case of a modular setup has to fulfill three functionalities. Primarily, forces shall be transferred across the structural linkage. As the pressure supply is positioned outside the shape-variable structure, the connection has to enable the fluid transfer. In case of defects or for maintenance, the connection has to be detachable. For the variable-camber wing device, these demands are satisfied by a form-locking groove profile. The shape for this profile is based on the profile 5 from item industrial technology.

2.4 Sealing and pressurization

The application of internal pressure is only realizable with a pressure-tight sealing concept for the cell axial direction. Such a cell closure has to ensure a constant pressurization of the complete cell compound, at cell sides, hinges and edge regions. It has to bear significant axial forces and simultaneously has to permit or even support cross-sectional deformations. Solving conflicting goals regarding its stiffness properties is further complicated by geometrical boundary conditions from neighbored cells or a changing cross section for each cell. The DSEC concept (*deformation supportive end cap*) is developed to provide a remedy for the need of such a sealing for PACS. The cell closure, its connection to the cell body and the design and dimensioning of the fluid flow are presented in the following chapter.

2.4.1 Cell closure

The shape-variable structure for the areal closure of the cells' apertures is named the cell closure. The concept for this essential structural element only enables the realization of PACS and widely influences the efficiency and accuracy of deformation. The detailed results on the cell closure are presented in a separate work [17]. After a particular requirement analysis and a listing of existing and novel potential solutions, the mechanism of action, the geometry creation and property analysis is performed. For the holistic design of PACS a summary of this underlying work on shape-variable seals and specifically on the DSEC shall be given.
As it can be seen in Figure 16 the cell closure is loaded with huge rotational distortions in the regions of the flexure hinges, and translational deformations due to the cell's volumetric expansion. Compared to the discrete positioning of rotational deformation in the cell body, the amount and combination of deformation mechanisms recommend utilizing the whole available closure surface for carrying the resulting strains. The design of a DSEC, equally to a single PACS cell, bases on two states of shape, the manufacturing state $st0$ and deformed state $stn = st1$ for the target state of shape $n = 1$. For the deformed state, the DSEC contour is identical with the contour of the asymptotically deformed cell. As the pressure-induced forces are directed to distort the DSEC into state $st1$, the pressure-dependent deformation behavior of cell and cell closure are comparable. Besides the specific control of pressure induced deformation, the target shape of the DSEC at $st1$ is conceived to approximate isotensoid geometry. Structural stresses are thus minimized for the state of asymptotic cell deformation.

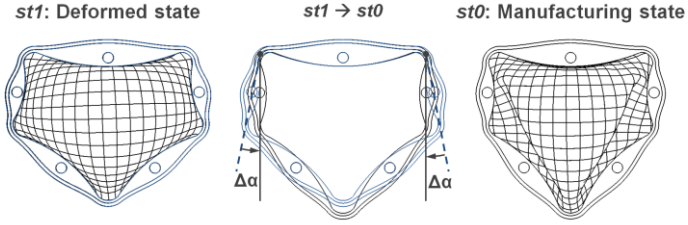

Figure 16: Shape of DSEC and underlying cell structure for the two design states of deformation

The conceptual work on the DSEC is followed by a characterization of its pressure dependent deformation behavior. Figure 17 illustrates the analogy of functionality for cell and sealing, though the DSEC structure is double-curved compared to the PACS and acts in the three dimensional room. The possibility of reaching even larger deformations than that of the underlying cell is shown by the implementation of the overdriven DSEC (cf. Figure 17, DSEC_OV). The basic method for creating this geometry is identical. Instead of using the equilibrium state of shape of the cell contour for $st1$, the contour's deformation is extrapolated by the factor 1.25.

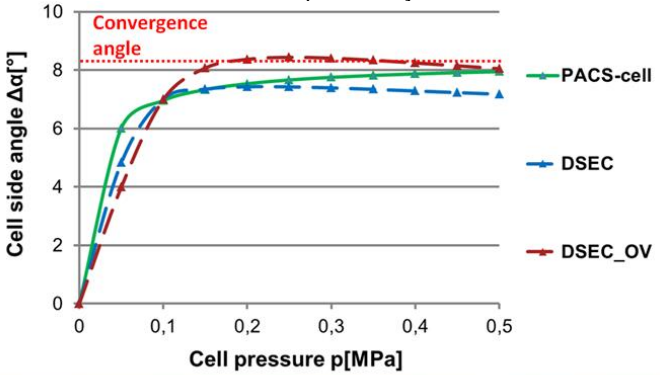

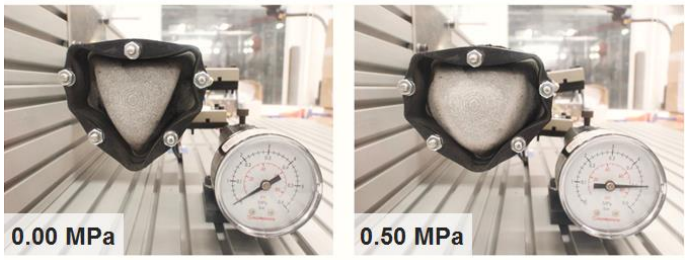

Figure 17: Results from numerical computations and experimental test setup for the characterization of DSEC

The basic method for creating this geometry is identical. Instead of using the equilibrium state of shape of the cell contour for $st1$, the contour's deformation is extrapolated by the factor 1.25.

2.4.2 Sealing and fluid flow

The pressure-tight sealing between cell body and closure is conceived as gasket seal. As the top left depiction of Figure 18 shows, the closure and gasket are designed as an integral membrane. The clamping of the gasket is realized by an additional segment, featuring the same cross section as the cell body, which can be bolted to the cell compound. The axial forces from the pressured closure as well as the preload forces for sealing the gasket have to be borne by screws, which are positioned to utilize the increased wall thickness of the cell sides.
The concept relies on the contact pressure between the join partners. Apart from hinge areas and thin-walled cell sides leakage could be observed at regions where the required contact pressure cannot be applied. In preliminary investigations, especially the bore holes for bolts are found to be a source for loss of fluid and therefor pressure. For this reason the gasket concept is enhanced by a sealing bead along the contour of each cell. Figure 18 shows the resulting design which increases the local clamping force equally to an O-ring seal and thus leads to a complete pressure-proof solution.
A non-moving pressure port at the interface structure prevents the pressure lines from abrasion and folding under operating conditions. One pressure port per cell row is sufficient and reduces interfaces to the shape-variable structure. The fluid transfer between the cells is realized internally (cf. Figure 18). A modular PACS application may profit from a second pressure port at the end of each cell row to transfer the fluid to the next PACS segment.
For reasons of accessibility the pressure port is positioned at the mounting frame. The same sealing concept as for the cell closure was applied to ensure tightness.

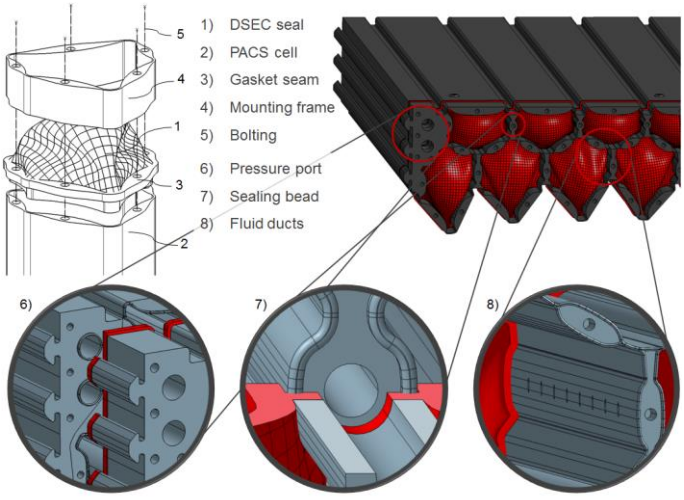

Figure 18: Sealing between DSEC and cell body and fluid transfer to PACS device and between individual cells

The design of the PACS is elaborated to a fully functional three-dimensional model. The necessary preparations for manufacturing a PACS prototype are thus made.

2.5 Realization

The three-dimensional geometries of the PACS cell body, the closure membrane and the appropriated mounting frame are defined within the recent design steps. The manufacturing and assembly of these elements is non-trivial and may have repercussions on the design. In the following, eligible manufacturing processes and assembly strategies are listed and assessed according to the underlying demand analysis.

2.5.1 Manufacturing

Although an integral manufacturing of cell body and closure is conceivable with concepts which are not in need of a third element like the mounting frame, the manufacturing issues are discussed on the basis of the geometry presented in chapter 2.4. The main requirements which are defined in the subsequent demand analysis are transferable. The objective of this chapter, in addition to presenting and evaluating suitable manufacturing processes, is to point out the critical issues with this subject.

2.5.1.1 Cell compound

The manufacturing demands for the cell compound structure can be divided into cross-sectional in-plane and out of plane challenges. Demands on the most heavily loaded hinge elements (requirement number 1: R_C1) concern the geometrical accuracy, which influences the stiffness and strength properties of PACS and the joint strength for connecting hinges with cell sides. Regarding equation (3), a change in thickness affects the hinge stiffness with the third power. A deviation η_t of more than 10 % shall thus not be exceeded. Although the asymptotic deformation is not modified for multiple stiffness values, the deformation phase is influenced heavily. The results of doubling or halving of hinge stiffness is presented in [16]. Draft angles, necessary for casting processes, even for scales below 3° are not tolerable regarding this demand. Stress maximums due to local changes of wall thickness also have to be avoided. Demands on the manufacturing of cell sides (R_C2) are subordinate. The geometrical accuracy at cell side regions is less critical for deformational behavior and, due to the freely selectable cell side safety factor SF_{CS}, for stress considerations. Huge thickness ratios between hinges and cell sides, of up to 1:5 for the given use case are problematic for some production methods.
Out-of-plane issues are given by warpage, the cell compound dimension, and processible material. Production-induced deformation (R_C3) results in local geometrical inaccuracy but also in global deviation. In the xy-plane it causes variations towards the targeted structural behavior. Warpage may affect the cross-sectional as well as the three-dimensional geometry. By contrast a curvature of the hinges in the cell axial direction leads to malfunction of the whole structure. The cross-sectional dimensions of the PACS and the cell length (R_C4), which is below $d = 1e3\ mm$ for the first demonstrators, may constitute problems for the manufacturing of a PACS device like for the variable-camber wing. For a span of several meters, a longitudinal segmentation is possible. Regarding system weight and complexity, segmentation however is unfavorable. Moreover, a manufacturing process is in general only suitable for a group of materials (R_C5). For the selection of this process, the conceived material thus has to be considered. The manufacturing process is rated according to the relevance of the applicable material for PACS (see chapter 2.1.2).
Optional requirements are defined in addition to the so far described imperative demands as they increase the significance of the available processes but do not state eliminatory criteria. The tightness of the cell body (R_C6) should optimally be given without additional rework or sealing elements. The fluid ducts (R_C7), which cause undercuts, are preferably integrated without additional manufacturing steps. The necessary efforts and costs for the production of a single PACS demonstrator (R_C8) or a large number of cell structures (R_C9) is a critical criterion for the selection of a convenient process.

Besides the depth of the cell compound, the flexibility of the resulting structure causes difficulties particularly in cutting processes. The experiences with PACS demonstrators further show that repair is expensive and especially for inlying cell sides or hinges the accessibility is limited.

A selection of suitable manufacturing processes and their evaluation with respect to the application for PACS is given in Table 2. For the underlined processes, either prototypes are built first, or experiences by manufacturing simulations are collected (extrusion, injection molding). The processes are rated on the basis of the demand analysis. ++ means that the particular requirement is completely fulfilled, -- stands for non-performance. A weighting factor is not applied since the importance of the single criterions depends on the specific needs. For the functionality of a PACS, the demands R6, R7 and R9 are subordinate. The high value of a prompt and cost-efficient production however was decisive for choosing the Selective Laser Sintering (SLS) process for the implementation of the double row PACS demonstrator, which is described in chapter 4.
The best solution in the unweighted evaluation of manufacturing processes is bonding. The bonded PACS structure profits from the separate selection of semi-finished products for cell sides and hinges. Besides the possibility of processing thin foils and sheets that can be produced with high accuracy, almost any material combinations are viable. PACS with lightweight sandwich cell sides, which consist of a foam core that is covered by Fiber Reinforced Plastics (FRP) face sheets can exemplarily be realized. A pure FRP process is used to manufacture the first single row PACS demonstrator [16]. For series production, this process is cost-intensive. With the advantage of higher joint strength at the expense of limited choice of materials, the laser welding process underlies the bonding concept. The discussion of solutions for manufacturing the cell compound structure is closed with the SLS process. As this variant profits from cost-efficient single item production and the possibility of the integral manufacturing of the fluid duct, the disadvantage of inferior materials is accepted for the implementation of prototypes.

Table 2: Evaluation of manufacturing processes for cell compound according to underlying demand analysis; (SLM: Selective Laser Melting; SLA: Stereolithography; FDM: Fused Deposition Modeling; EDM: Electrical Discharge Machining) [29], [30]

Nr.	Manufacturing process	Performance w.r.t. requirements									Sum
		R_C1	R_C2	R_C3	R_C4	R_C5	R_C6	R_C7	R_C8	R_C9	
1	Bonding	+	++	++	++	+	+	+	-	+	10
2	**FRP Prepreg**	++	++	+	++	++	++	0	0	--	9
3	Laser welding	++	++	+	+	0	+	+	--	+	7
4	**SLS**	+	+	+	0	-	+	++	++	-	6
5	**FDM**	+	++	++	0	--	0	+	++	-	5
6	SLA	+	+	++	0	--	+	+	++	-	5
7	**Water cutting**	-	++	++	0	0	--	0	++	+	4
8	**EDM**	++	++	++	-	+	++	--	0	--	4
9	**Laser cutting**	--	++	++	0	0	--	0	++	+	3
10	**SLM**	+	+	0	-	-	+	++	+	-	3
11	Investment Casting	-	--	+	-	0	++	++	-	+	1
12	**Extrusion**	0	-	-	++	0	++	--	--	++	0
13	**Injection Molding**	0	--	--	0	0	++	-	--	++	-3

With the selection and evaluation of suitable production processes for the PACS cell compound structure, the main part of a real-life PACS can be manufactured.

2.5.1.2 Cell closure

Demands on geometrical accuracy of the closure and sealing structure (R_S1) are essential for the resulting stiffness and strength properties. Production-induced deformations may cause unacceptable shrinkage and warpage. Remedy can be provided by considering these deformations in the tooling design. The manufacturable dimensions (R_S2) limit the maximum size of the cell closure. Within the group of elastomers, materials with a high ratio of strength to stiffness are preferable. A process which allows using several and mechanically advantageous materials is privileged (R_S3). Depending on the applicable material and manufacturing process, the pressure tightness (R_S4) is given either directly and without rework with the primary shaping or in a separate process. The suitability for single (R_S5) and series production (R_S6) completes the demands on the appropriate manufacturing process.
For the manufacturing of the closure membrane, a process that allows geometrical undercuts is inevitable. The applicable materials for shape-variable seals are currently limited to elastomers for reasons of functionality [17]. In contrary to the manufacturing of the cell compound, the demolding is thus realizable for rigid molds without sliders.

With the most suitable process (cf. Table 3), the injection molding, various material systems are workable. Thermoplastic elastomers like Thermoplastic Polyurethane (TPU) are processed above their melting temperature, what causes warpage due to thermal shrinkage. With using non-thermoplastic materials like Nitrile Butadiene Rubber (NBR) or Ethylene Propylene Diene Rubber (EPDM) this issue can be circumvented. The rapid prototyping processes SLS and FDM are limited to the processing of particular materials but profit from efficient single part production.

Table 3: Evaluation of manufacturing processes for cell closure according to underlying demand analysis

Nr.	Manufacturing process	Performance w.r.t. requirements						Sum
		R_S1	R_S2	R_S3	R_S4	R_S5	R_S6	
1	**Injection Molding**	+	+	++	++	-	++	7
2	**SLS**	+	+	-	+	++	-	3
3	FDM	+	+	--	-	++	-	0

For the realization of slightly loaded single functional demonstrators the SLS process is the preferential manufacturing process for cell closure structures.

2.5.2 Assembly

The herein presented PACS device is designed differentially. It consists of the three elements cell compound, cell closure and mounting frame. The concept for the assembly of these components and the required geometrical changes complete the holistic design for PACS.
Three assembly concepts were identified to be convenient for the application of PACS. Welding of cell body and closure leads to a pressure-tight connection with minor or without additional material and mass. The similarity of cell compound and closure material is premise for this connection method. Transitions between thin hinge regions and cell closures with increased wall thickness together with a small joining surface disadvantages the butt joint compared to the lap joint (see Figure 19). The lap joint whereas yields the disadvantage of hinge stiffening.
The possibility of connecting components made of different materials is given by the bonding process. The joint stresses [31] of the stronger lap joint can be calculated by

(34) $\tau^*_{C,max} = \sigma_{10}\sqrt{\frac{G_C t_1}{E_1 t_C(1+\psi)}}$, with

(35) $\psi = \frac{E_1 t_1}{E_2 t_2} < 1.$

$\tau^*_{C,max}$ is the maximum shear stress within a bonded joint due to the joint partner stresses σ_{10}, which are parallel to the adhesive layer. The shear stiffness of the cohesive film is G_C, its thickness is t_C. E_1 and E_2 are the elastic modules and t_1 and t_2 the wall thicknesses of the joint partners that are used to compute the ratio of longitudinal stiffness ψ. The elastic moduli of the joint partners significantly influence the strength of the connection. For the use of elastomeric material the load bearing flange length l^* is small:

(36) $l^* = 5\sqrt{\frac{E_1 t_1 t_C}{G_C(1+\psi)}}.$

The maximum pressure has to be reduced in order to be bearable. The stiffer the respective joint partners, the more convenient are bonded joints.

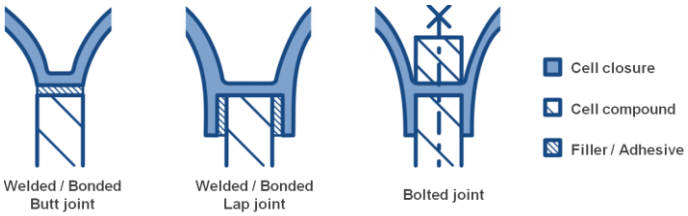

Figure 19: Assembly concepts for connecting cell compound and cell closure

In contrast to bonded and welded joints, the utilization of bolted joints does not limit the material selection for the joint partners. Based on the sealing concept presented in chapter 2.4.2, a pressure-tight connection is conceived, which utilizes the elastic properties of the cell closure. The disadvantage about this variant is that a secondary structure, the mounting frame, is needed to distribute local attachment forces. In addition to pressure-induced forces, the bolted joint thus has to bear forces that are required to achieve the sealing effect. Details about the occurring forces with this connection concept are given in [17]. The necessary diameter D_B of a bolt [32] can be calculated according to

(37) $D_B = \sqrt{\frac{A_B}{\pi}} = \sqrt{\frac{(F_c + F_{op}) k_A \kappa}{\pi R_B}}.$

The clamping force F_c and the operating force F_{op} have to be borne by a bolt of strength R_B for a tightening factor k_A and the friction based reduction factor κ. As depicted in Figure 18 it can be seen that the wall thickness of the cell sides is increased according to the resulting bolt size, to enable this connection.

3 Evaluation by FEM-based simulation of variable-camber wing structure

The numerically calculated results on the basis of the truss model shall be evaluated by computations, using the commercial FEM software *Ansys*. The pressure-dependent deformation behavior and the according structural stresses are investigated for the variable-camber wing PACS device in a two-dimensional consideration. The results of this investigation enable to determine deviations between truss and FEM model and thus allow evaluating the validity of the underlying assumptions.

3.1 FEM model for cross-sectional geometry

In equality to the truss model, the FEM model is implemented in the two-dimensional space. The cross-sectional PACS area is modeled with linear Plane182 elements. The sensitivity analysis presented in Figure 20 is processed for the pressure values $p_{int,1} = 1.0\ MPa$ and $p_{int,2} = 0.0\ MPa$, which causes maximum deformation. As the deviation of the cell side orientation angle $\Delta\beta$ is used to examine the convergence behavior, the worst case is thus considered. The sensitivity analysis leads to a necessary element edge length for hinge regions of $0.05\ mm$. The computational expense, shown in Figure 20, is normalized with the respective value of the selected element size.
The initial, unloaded state of the PACS model is depicted in Figure 21 and shows the adapted element resolution. Divided in hinge and cell side regions the element size is controlled in dependency on the wall thickness. A ratio of element size of 1:10 is chosen in accordance to the variance between hinge and mean cell side thickness. It allows reaching the required resolution for the thin-walled flexure hinges and simultaneously save computation time for cell sides. Compared to the overall size of the structure of $435\ x\ 100\ mm^2$ the hinge element edge length of $0.05\ mm$ causes high resolution and, with 76.2e3 elements, huge computational expense. Hinge elements are represented by four to five shell elements and cell sides, depending on their length-based thickness, by eight or less elements. The geometrically non-linear deformation is considered by an iterative solution strategy.

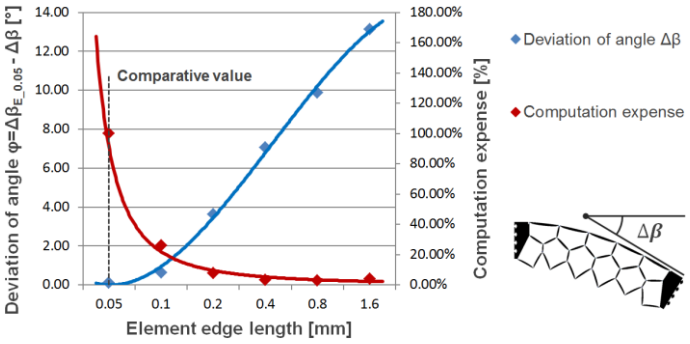

Figure 20: Sensitivity analysis for FEM model

Three different pressure ratios are used to compare the outcomes of the truss model and the FEM model: the exclusive pressurization of the first cell row (I), the pressurization of only the second row (II) and the uniform loading of both rows (III). External loads and forces of inertia are neglected for these investigations in order to provide consistence with the load set for the design point. Besides the design pressure ratio also the load states which lead to the maximum deformation are thus used for the comparison of computational results.

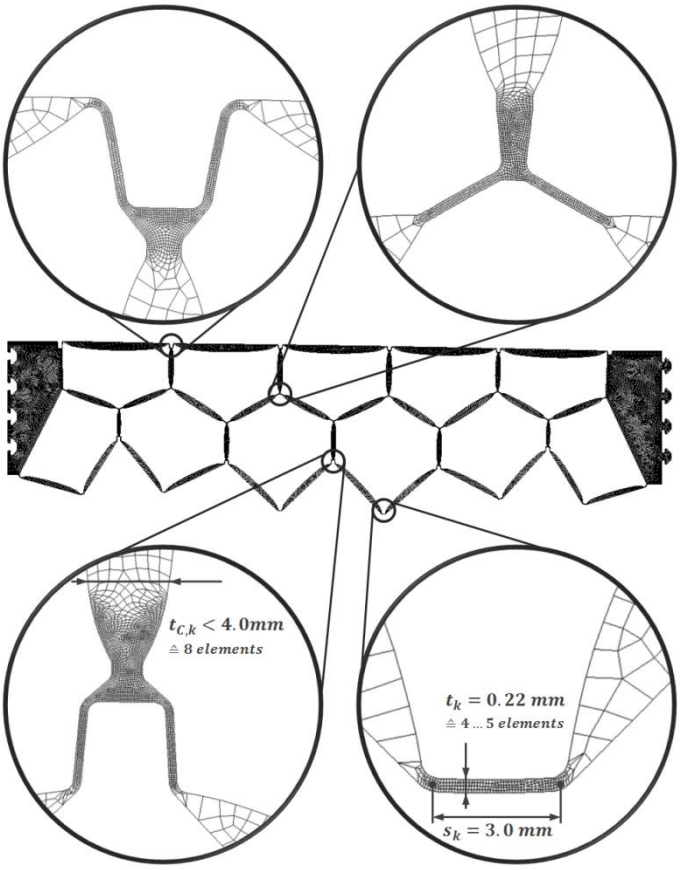

Figure 21: FEM model for variable-camber wing PACS device

3.2 Deformation and stress results

The primary target of the holistic design for PACS is to provide the necessary methods for realizing a structure that deforms into a predefined shape at a specific load state. The quality of the two-dimensional structure that results from the form-finding process is measured by evaluating the outcomes of the FEM model. In equality to the evaluation shown in Figure 20 the angle $\Delta\beta$, which describes the rotation of the non-fixed connection structure, is shown in Figure 22 for various pressure settings. As this rotation angle results from the summation of the deflection of the complete cell compound it can be used to compute the cumulative deformational error.

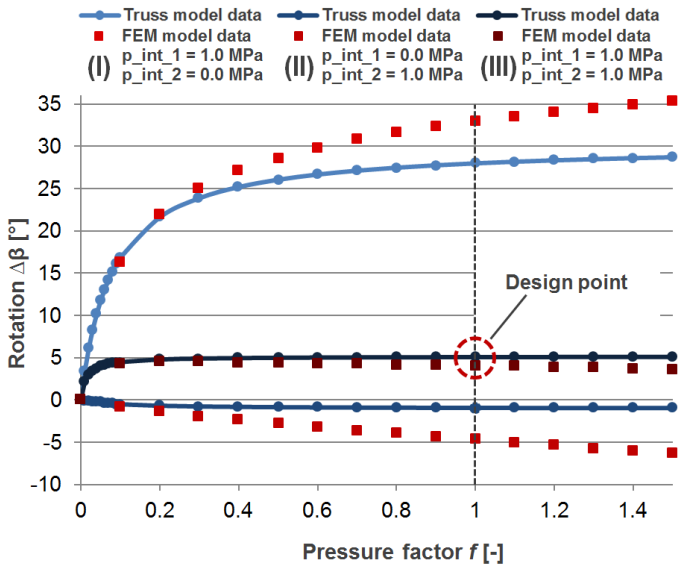

Figure 22: Comparison of computational results for pressure-dependent deformations from truss and FEM model

It can be seen that the deviations between truss and FEM model increase for rising pressure values. Depending on the actual load set, the angle $\Delta\beta$, extracted from the FEM model, exceeds or falls below the results from the truss model. For the pressure factor $f = 1$, a deviation of $\Delta\beta_{dev,I} = 4.99°$, $\Delta\beta_{dev,II} = 3.74°$, and $\Delta\beta_{dev,III} = 1.05°$ is measured for the three load states. Small deviations for the load set of the design point (III) attest the efficiency of the presented design process. The reasons for the deviations and divergence of the resulting values are discussed in the following (see chapter 3.3).

The length-dependent cell side thickness is calculated according to equation (29) with a safety factor of $SF_{CS} = 8$. The analytical dimensioning leads to a constant stress distribution in the extreme fiber of $\sigma_{CS,max,ana} = 150\ MPa$. Figure 23 includes the FEM-based stress results for the two marked cell sides. Between hinges and central cell side regions with controlled thickness, a geometrical transition zone causes stress increases. For the major part of the cell sides, which is dimensioned according to equation (29), the stress distribution over cell side length, as well as the extreme fiber value are constant and consist with the underlying analytics.

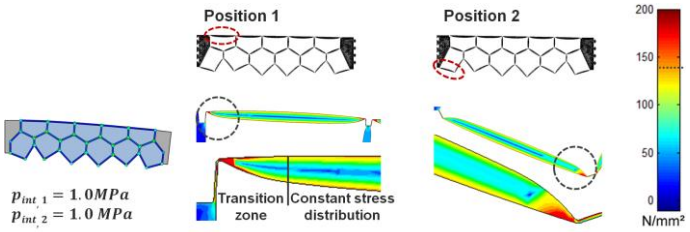

Figure 23: Stresses in cell sides for upper and lower cell row

Equally to the global deformation, the deviation of structural stresses rises with the amount of pressure. For the three examined pressure ratios it is minimal for load state (III). For the pressure factor $f = 1$, the global maximum stresses of truss and FEM model deviate by $\Delta\sigma_{vM,I} = 1937.69$ MPa, $\Delta\sigma_{vM,II} = 1950.59$ MPa and $\Delta\sigma_{vM,III} = 273.35$ MPa. Local stress peaks surpass the strength value of the utilized GFRP material HexPly913-EC9756.

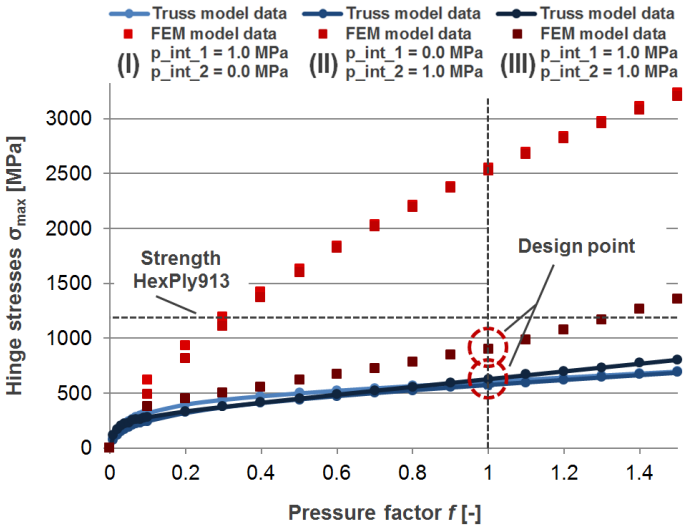

Figure 24: Comparison of computational results for pressure-dependent stresses from truss and FEM model

For the design pressure state the stress distribution is homogeneous over the hinge length. As shown in Figure 25, both positions for the uniform pressurization of the two cell rows show smooth stress gradients. The maximum stress of $\sigma_{vM,max,III} = 901.01$ MPa results for $p_{int,1} = p_{int,2} = 1.0\ MPa$.

The maximum value for the stress coloring is set to this value in order to show the effects of the load induced PACS design. As the hinge orientation and curvature is designed for one single load state, the cross-sectional geometry is non-optimal for a variation of internal or external forces. For the off-design pressure ratio (I), at position two, the direction of primary stresses does not correspond to the hinge orientation. The global tension peak of $\sigma_{vM,max,I} = 2541.61\,\mathrm{MPa}$ surpasses the design point value by the factor 2.82. For the pressure ratio (II) the maximum stress is $\sigma_{vM,max,II} = 2525.10\,\mathrm{MPa}$.

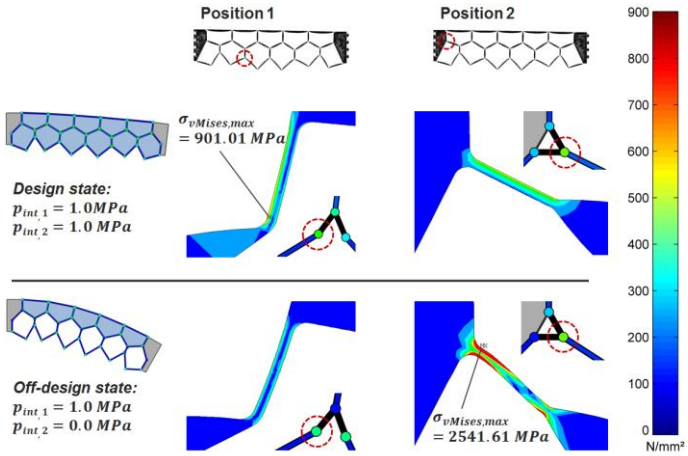

Figure 25: Stress distribution for two pressure states at the positions of maximum stresses

3.3 Discussion of deviations

The deviation of deformations is caused by assumptions for hinge and cell side elements in the truss model and the related creation of the cross-sectional geometry. Simplifications due to the concentration of flexure hinges to a one-dimensional joint in the truss model leads to five possible sources for variations:

1-a) Hinge curvature does not suit principal stresses
1-b) Hinge orientation does not suit principal stresses
1-c) Assumed hinge length does not include transition zone
1-d) Elongation of flexure hinge not included
1-e) Migrating of effective hinge positions

The mentioned reasons all refer to the utilization of flexure hinges for PACS, which profit from advantages like pressure tightness and integral design. These arguments lead to a change of the stiffness behavior. As shown in chapter 2.2, the pressure-dependent behavior of PACS can be varied by changing the hinge stiffnesses. The consideration of pressure- and deformation-dependent stiffness of flexure hinges is currently not implemented in their physical description within the truss model. Another effect is the relocation of effective hinge positions with respect to the neighboring cell sides, resulting from 1-c) to 1-e). Since the computation of deformations bases on the length of cell sides, a repositioning of hinge elements inevitably influences these results. The divergent deformation course and the according pressure dependency of deviations which is shown in Figure 22 confirm these issues.
With the modeling of cell sides as rigid beams within the truss model, the following effects are not included:

2-a) Elongation of cell sides
2-b) Bending of cell sides

In equality to the arguments 1-c) to 1-e), the cell-side-based effects 2-a) to 2-b) influence the optimization parameters of the form finding process, the cell side lengths. For the resulting deformations, the reactions of cell sides on the applied forces are additional factors of influence. With the selection of the GFRP material HexPly913-EC9756, the cell side dependent effects are reduced due to high tensile stiffness. Values of less than 0.1 % of cell side longitudinal strain are achieved by a high elastic modulus and a huge safety factor SF_{CS}.

Stress peaks as depicted in Figure 25 are concentrated at flexure hinges. The load-based cross-sectional design produces relief for only one design state. A change in loading and deformation, which leads to lateral forces, causes irregular stresses within hinge elements, which continues in the transition zone between hinge and cell side. The stress distribution in cell sides is regular and can be adequately controlled according to equation (29), by dimensioning the cell side thickness of each cell for the maximum applicable pressure. Experiences with former demonstrators [16], [17] and the subsequently presented implementation (cf. chapter 4) give rise to the assumption that an overload of a limited geometrical region does not endanger structural integrity. Reason for this is the redistribution of structural loads due to local plasticization. The relevance of local stress peaks at flexure hinges for the global structural strength especially under consideration of fatigue issues is part of the future work. It shall be noticed that for counteracting this overstressing, the pressure level or the target deformations can be reduced (cf. Figure 24). Blocking forces and actuation strains, which specify the efficiency of an actuator, depend on these parameters and may thus be reduced.

Though the internal loads on the structure for load set (III) overweight those of the other two pressure ratios, the results of truss and FEM model match significantly better. Hence the global increase of loads is not the decisive factor for differences. It could be shown that the load-dependent design of the PACS's cross section provides the desired results. A design state, which involves the complete load envelope of a PACS device would profit from a reduction of stress peaks in a global consideration.

4 Evaluation by experimental testing of variable surface demonstrator

Based on the described strategy for the holistic design of PACS, a real-life demonstrator is designed, manufactured and experimentally examined for the experimental evaluation of the holistic design process for PACS.
For the investigation of deviations between truss model and FEM-based computations additional material-dependent influences are avoided by using HexPly913-EC9756. In contrast to the variable-camber wing PACS, the herein presented structure is manufactured from the polymeric material PA2200. As discussed in chapter 2.5.1 the SLS process allows designing and manufacturing also small quantities of integral PACS prototypes. Disadvantages regarding deformational accuracy with using a less appropriate plastic material (see chapter 2.1.2) are accepted for the purpose of demonstrating the proof of concept. Due to the changed objectives and material, the shape of the PACS is modified. Figure 26 depicts the design process and the resulting geometry of the demonstrator.

4.1 Objectives

The realization of a PACS device validates the underlying methods, regarding the dimensioning of the truss structure, up to the manufacturability and assembly. Manufacturing processes are evaluated for the single-part production of a double row PACS cell compound and for the related closure structure. The fluid flow and sealing solution are evaluated as well as the stiffness influences from the cell closure membrane, after the successful assembly.

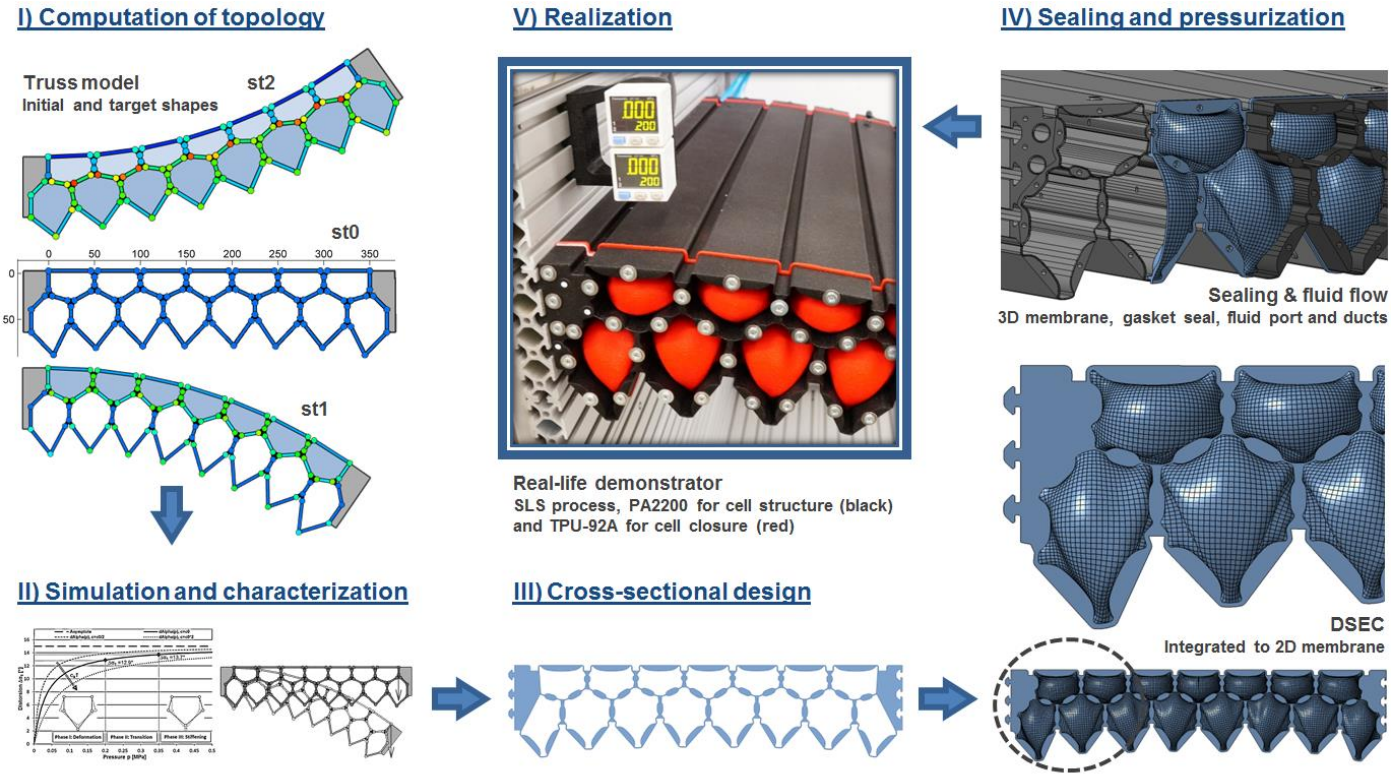

Figure 26: Process chain for holistic design at the exemplary structure of the variable surface demonstrator

As the major property of the cell compound, the pressure-dependent deformation behavior is investigated for a PACS that is built of seven pentagonal and eight hexagonal cells. The application of point loads verifies the computational models regarding external forces.
Three sources of data are used to compare the results, the truss model, a two-dimensional FEM model and the experimental test. The differences between truss and FEM model are discussed in chapter 3.3 for the use of the highly rigid material HexPly913-EC9756. Important additional information is to be obtained from the comparison of experimental and FEM-based results. The cell closure membrane and its periphery, the mounting frame, boreholes and screws as well as the fluid ducts are not considered in the two-dimensional FEM computations. The effects of this secondary PACS structure are investigated.
The implementation of the shape-variable surface demonstrator further examines the concept for the possibility of realizing a modular structure and gives an outlook for potential applications.

4.2 Realization

For the implementation of a functional demonstrator for the conceptual validation of the described process chain, a time and cost-efficient solution is advantageous. The manufacturing process SLS is beneficial for single-part production and allows the integration of fluid ducts. The limited alternatives regarding the material selection cause a restriction of the maximum bearable deformation and pressure loads. With the material PA2200 (cf. Table 1), a hinge length of $s_{VS} = 4mm$, an average cell diameter of $D_{VS} = 50mm$ and a maximum hinge distortion of $\Delta\alpha_{VS,max} = 15.46°$ the maximum operating pressure for the variable surface demonstrator is $p_{VS,max} = 0.49MPa$, according to equation (2). A preliminary test with a PACS consisting of two cells confirms this value. Due to the non-linear stiffness properties of PA2200, which leads to a reduction of stress peaks, a failure value of $p_{VS,max,exp} = 0.6MPa$ is reached in this test.

The PACS demonstrator is conceived to consist of seven pentagonal and eight hexagonal cells, describes a flat surface with its upper cell sides for the initial state and has an overall length of $l_{VS} = 400\ mm$. The target shapes are described by a circular arc with an angular deflection of the upmost cell sides per pentagonal cell of $\Delta\alpha_{n,t1} = 5°$ for the pressure state one, with $p_{int,1,t1} = 0.5\ MPa$ and $p_{int,2,t1} = 0.0\ MPa$, and $\Delta\alpha_{n,t2} = -5°$ for the pressure state two, with $p_{int,1,t2} = 0.1\ MPa$ and $p_{int,2,t2} = 0.5\ MPa$ (cf. Figure 26). The shape-variable structure is supported at one end. Forces of inertia and further external loads are considered in the characterization step.
The cross-sectional design is generated using a uniform hinge thickness of $t_{\boldsymbol{k}} = 0.7\ mm$. Functional flexure hinges can be guaranteed for thicknesses from $0.65\ mm$ in the SLS process with an *EOS P 760* laser sintering machine. For the pressure-tight sealing between cell compound and closure, an increase of hinge thickness is advantageous as it allows for a more durable sealing bulge. The integration of screw holes limits the minimum cell side wall thickness to $t_{C,min} = 6\ mm$. Subsequent to the form finding process for the DSECs, according to [17], the fluid ports and ducts are implemented in the cell compound and closure, to realize the pressure connectivity and the respective air flow of a pneumatic hose with 6 mm of internal diameter.
The process chain for designing the variable surface demonstrator is summarized in Figure 26. The CAD models are created with the commercial software CATIA V5R21. The real-life implementation of the structure is shown within the test setup for the subsequent investigations in Figure 28.

4.3 Experiment evaluation of computational data

A two-dimensional FEM model, basing on the cross section of the modular PACS unit, is implemented. It provides the basic information for the comparison of the pressure-dependent deformation behavior of the cross section of PACS in a 2D consideration and the behavior of the real-life structure with cell closure membrane and fluid ducts.

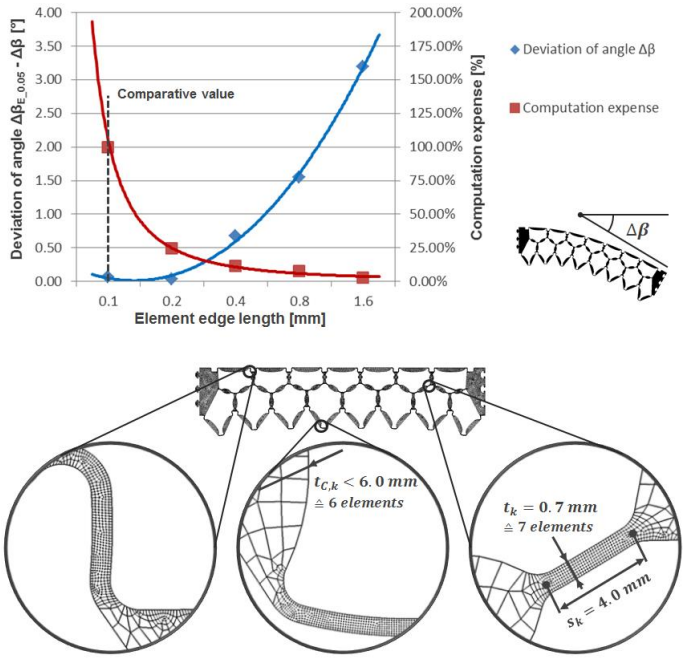

Figure 27: Sensitivity analysis for adjusting the element size and resulting FEM model

The element sensitivity analysis depicted in Figure 27 leads to an element edge length of $0.1\,mm$ for hinges and $1.0\,mm$ for cell sides. In the appropriate FEM model the functional hinge regions are described by at least seven and the cell sides by eight or less shell elements.

The experimental setup for measuring the related data from the real-life implementation is depicted in Figure 28. The test specimen is attached to the test bench at one side and equipped with *Althen AIT710-0101-60* inclinometers for measuring angular deflection at its opposing end. At the back of the depicted mounting wall, two *B&B Thermotechnik DRTR-AL-10V-R10B* pressure gauges evaluate the actual pressurization state at the pressure holes and provide the necessary information for controlling the fluid transfer at the pressure ports. The analogue data from pressure gauges and inclinometers is received by a *National Instruments CompactRIO* and is processed with *LabView*. The pressure regulator is a *SMC ITV0031-2BL-Q*. The accessory pressure gauges *Panasonic DP102EP* with digital display at the front of the test bench afford visual feedback.

In addition to the evaluation of local distortions, the optical measurement system *GOM Atos* is used to digitize the upper surface of the PACS at specific load states (see Figure 28). The desired information resulting from this measurement technology is the surface deformation in the xy- and yz-plane. The xy-shape (1) evaluates and extends the information from the inclinometers, whereas the yz-shape (2) of the PACS indicates influences from the closure membrane on the global deformation behavior.

The specimen is loaded with the internal pressures $p_{int,1}$ and $p_{int,2}$ and the external point (2D) respectively line load (3D) F_{PL}. The maximum pressure is limited to 0.25 MPa for each cell row. Four attachments are used to distribute the external load evenly over the depth of the connection structure.

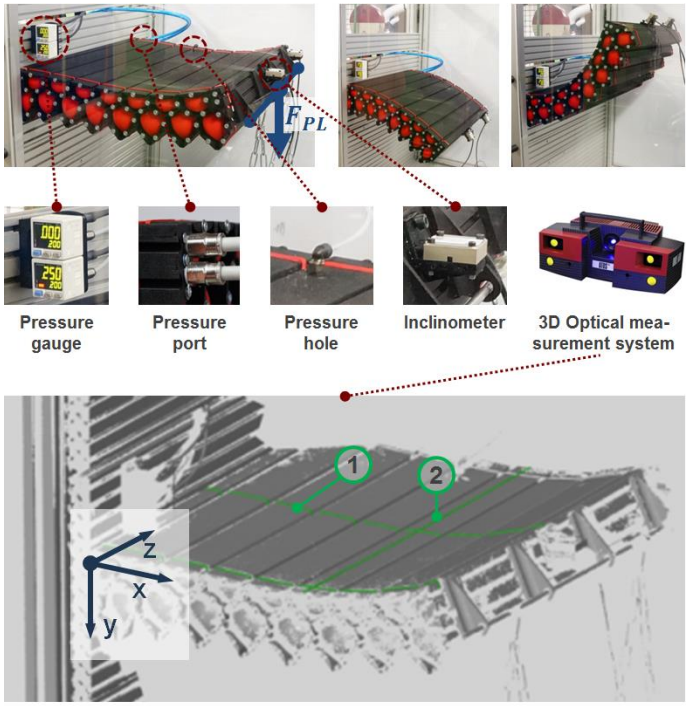

Figure 28: Modular unit of variable surface PACS demonstrator; test setup (top) and results from optical measurement (bottom)

The test procedure is divided into five stages. After the measuring of the deformational state of the unloaded structure, three different pressure ratios with five sub-steps each are investigated. With a constant pressure of $p_{int,2} = 0.25\,MPa$ applied to the cells of the second row, the effects of changing external loads on the deformation are examined finally. In equality to the examinations in chapter 3.2 the pressure ratio is kept constant within each stage, while the amount of pressure is altered by the pressure factor f. The rotation $\Delta\beta$ gives the distortion angle at the free end of the PACS device. Figure 29 summarizes the results from the truss, the FEM model and the experimental investigations.

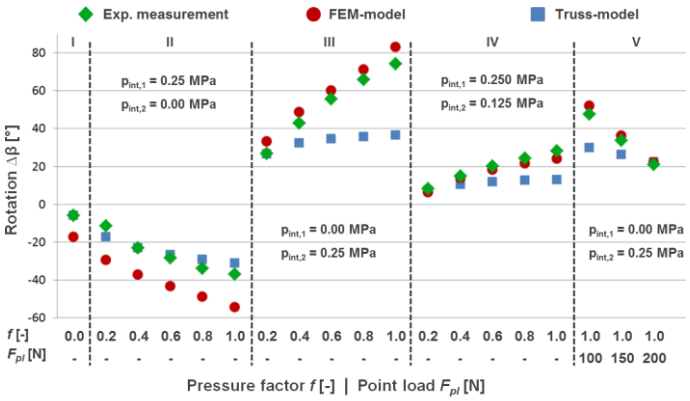

Figure 29: Rotational deformation at free end of the experimental PACS for different pressure settings and point loads

For the deviation analysis a three-dimensional measurement of the specimens' upper surface for two load states shall provide the information about the global deformational shape. The consideration of deviations between clamping and inclinometer in the xy-plane allows discarding and determining reasons for variances and demonstrates the applicability of the inclinometer data for the evaluation (see Figure 30). Measurements in the yz-plane are used to visualize the bending of the cell compound in cell axial direction and to quantify effects of the cell closure on the global deformations.

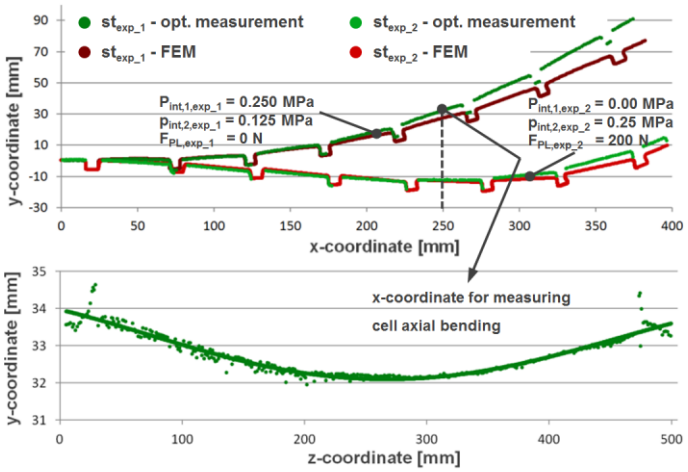

Figure 30: Optical measurement and comparison with FEM-based computations for xy- and yz-plane

The subsequent discussion of results evaluates the outcomes, identifies reasons for deviations and points the way ahead.

4.4 Discussion of results

Forces of inertia are included in both computational models in order to establish common conditions. Variances between the results from the truss and the FEM model thus have to be caused by the reasons described in chapter 3.3. As pressure loads are not yet applied to the structure, cell side elongation does not significantly affect the resulting distortion. A deviation of $\Delta\beta_{dev} = 11.24°$ can be obtained and is consequently caused by assumptions within the implementation of hinge elements in the truss model. The increase of this deviation with rising amounts of pressure, which are investigated in the test segments two to five (cf. Figure 29), verify the relevance of hinge and cell side effects for accuracy of the computational results. Variations between FEM data and the experimental values attest the influence of the cell closure on the overall deformation. As investigated in [17] the DSEC is designed to utilize the cell pressure to support deformation. For zero pressure, the membrane's stiffness leads to a reduction of the PACS's deformation. The related values can be extracted from Figure 29. It should be noted that the examined PACS structure shows a deformation hysteresis, which is due to the utilization of polymeric and elastomeric materials. A value of $\Delta\beta_{hys} = \pm 8°$ appeared for the unloaded structure. An increase of loads reduces the influence of flexure-hinge-based energy potentials on the deformation and thus the cause for this hysteresis. The plastic deformation of hinge elements is another effect that results from the utilization of flexure hinges, expands the theoretical deviation analysis in chapter 3.3 and is labeled with 1-f).

The experimental stages two to four show the known deviations between truss and FEM model. In contrary to the virtual variable-camber wing PACS device, the actual material PA2200 is of lower stiffness. The cell side effects 2-a) and 2-b) become more important. Together with the hinge-based influences, they affect the deformed shape of the PACS. Figure 29 shows an increase of deviations for rising deformations and cell pressures. The experimental angular distortion deceeds the FEM-based values for single-pressured rows and exceeds it for the pressurization of both cell rows. The reasons for this lie in the negligence of the closure membrane in the FEM model and can be summarized to

3-a) the stiffness of the closure membrane and
3-b) the pressure induced forces from the closure membrane.

Regarding the given results, it can be seen that the stiffness effects of the cell closure are maximal for the pressurization of the upper cell row. It reduces for the pressurization of the lower row and inverts for the fourth test stage, where both rows are pressurized. As mentioned previously, the neutral fiber of the PACS cantilever is represented by the upper cell sides. Stiffness effects from the second cell row result in higher momentums due to the larger lever arm of the underlying forces. For increasing pressure loads, the closure stiffness is compensated and exceeded by pressure-induced forces (3-b), what can be observed in test stage four. The exceedance is enabled by the present usage of an overdriven DSEC (cf. Figure 17, DSEC_OV), which is designed to cause a factor 1.5 of deformation compared to the underlying PACS cell. The results presented in Figure 17 confirm this relationship by providing the pressure-dependent deformation behavior of such a cell closures.

Starting from the loading conditions of stage three, the application of external point loads causes a reduction of deformations especially near the mounted end of the PACS (cf. Figure 28 and Figure 30). The deviations between truss and FEM model, depending on hinge and cell side deformations, as well as the variances of FEM data compared to experimental values, due to cell closure deformations, decrease. A divergent course is expected for a further rise of the point load, which would result in increasing deformations.

The verification of the PACS functionality in a segmented architecture, the demonstration of its shape-changing capabilities and the intermediate step towards a shape-changing airfoil is implemented by the demonstrator depicted in Figure 32. The modular device is assembled from two of the introduced and examined PA2200 PACS. Although the target shapes of the structure are designed for pressures of $p_{int,1,max} = p_{int,1,max} = 0.5\,MPa$ the manufacturing quality caused a limitation of the internal pressure to 0.2 MPa. The resulting structural shape of the experimental demonstrator for four pressure states can be compared with the respective computational outcomes in Figure 31.

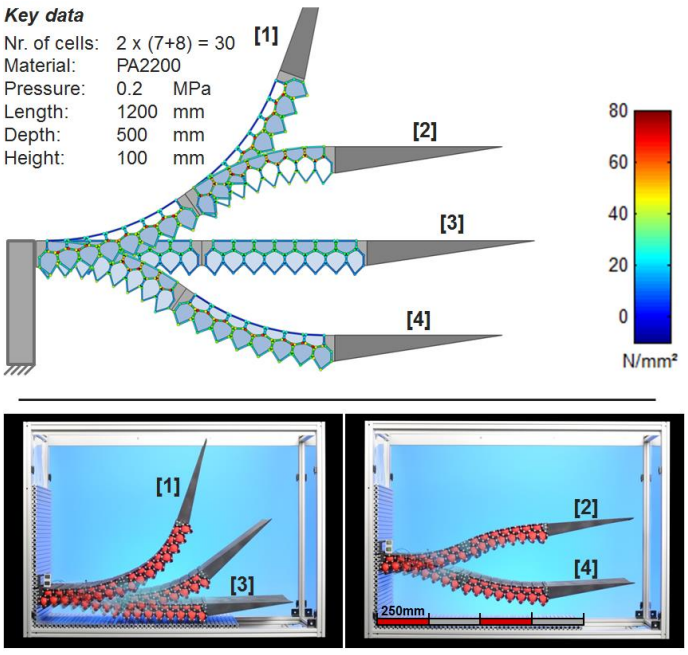

Figure 31: Computational deformation results and experimental test of the modular variable surface PACS demonstrator

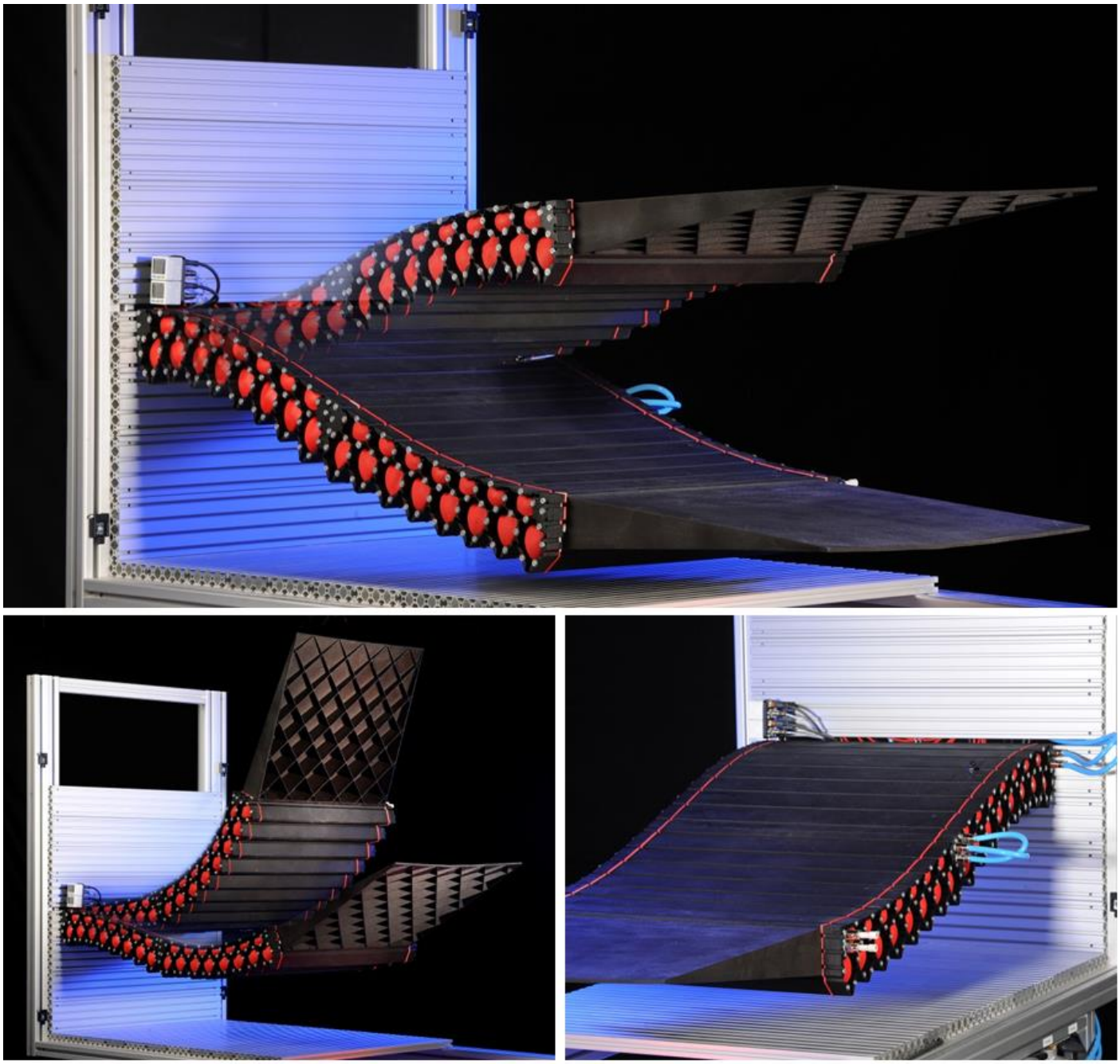

Figure 32: Modular PACS demonstrator for the realization of a shape-variable surface: length x depth x height = 1200 x 500 x 100 mm³; total mass = 9.2 kg; two pressure channels, maximum pressure = 0.2 MPa

Deviations regarding deformation and structural stresses of this prototype are uncovered within this work. The accordance of the pressure-dependent deformation behavior of a real-life PACS unit and the underlying form finding procedure strongly depends on the utilized materials as the varying results of chapter 3 and 4 show. Furthermore, the prospective work on PACS shall treat the discussed issues, concerning flexure hinges, cell sides and the cell closure membrane.

5 Conclusion

With knowledge about the holistic design process for PACS, the dimensioning of these shape-variable structures is advanced to exploit concept specific potentials. The ability of changing an initial manufacturing shape to multiple target shapes leads to additional loads within the structure, which can be borne best by materials with a high strength to stiffness ratio. A form-finding process is described at the exemplary application of a variable-camber wing, which considers conceptually necessary internal forces as well as external operational loads. The resulting two-dimensional truss model provides the capability to reach predefined target shapes under given load conditions for specific cell pressures and to move stepless between them. In the subsequently processed transfer to a cross-sectional design, structural loads provide the basic information for determining the thickness of cell sides, the position, orientation and curvature of flexure hinges. The two-dimensional geometry is computed by combining the stress-based geometry data with the information about the initial shape of the PACS. An efficient concept for sealing and cell closure is presented before manufacturing processes for cell compound and sealing

membrane are discussed. Especially for stiff materials, the resulting optimum wall thicknesses for flexure hinges of only several tenth of a millimeter cause manufacturing difficulties. An FEM-based simulation on the basis of the variable-camber wing application is processed in order to evaluate the outcomes from the truss model. It is shown that local load peaks exceed the analytically predicted stresses within the flexure hinges. The efficiency of the load-based cross-sectional design is confirmed through the reduction of stresses in the design state by the factor 2.82, compared to an off-design state. Regarding the accuracy of the computation of the pressure-dependent deformation behavior, a divergent course could be observed for increasing cell pressures. As the pressure loads cause structural strains at hinge and cell side elements, basic assumptions which are used in the truss model lead to deviations. Divided into hinge, cell side and cell closure influences, the reasons for stress peaks and deformational variances are revealed.
According to the introduced holistic design strategy for PACS, a real-life demonstrator is built, which provides the experimental data for the evaluation of the theoretical work. The comparison of computational results from truss and FEM model with measured data for multiple load states with only inertial and also point loads, shows good convergence near the design state, but also reveals open issues for the future work. The modular architecture allowed realizing a double row PACS with the dimensions 1200 x 500 x 100 mm³ in a SLS manufacturing process and evaluated the practicability of a segmented design.

6 Prospect

Further investigations on PACS shall illuminate four open issues. First, a more detailed implementation of the physical description of flexure hinges holds potentials to increase the accuracy of the truss model regarding deformations and local stress peaks. Second, the consideration of the elongation of cell sides due to axial and bending loads produces relief to currently made assumptions and allows computing the non-converging states of shape for increasing pressures. Third, the actual concept of pentagonal cells in the first cell row causes an inappropriate hinge orientation for the elements of the upper surface. Grooves at this aerodynamically interesting region, as well as sources for deformational deviances can be avoided by using a tetragonal basic structure. Forth, the concept of PACS shall be arranged within an aeronautical application for which a prototype is being built. The benefits of the concept within this application provide clarification about the potentials of PACS for future aeronautical use.

7 Appendix

The following data summarizes the computational data about the variable-camber wing PACS device for 0.6 to 0.9 of chord length of a NACA 0012 profile and a maximum deflection of $\beta_2 = 15°$. The utilized material the initial geometry and load states are defined prior to the form-finding process. Figure 33 holds global geometrical information, Table 4 lists point loads at the connection structure, Table 5 summarizes aerodynamic pressures and Table 6 gives the required information about initial cell side lengths. The resulting cell side lengths, which are modified in the form-finding process, are presented in Table 7. The variable cell sides are marked in italics to differentiate between those parameters and fixed ones that are predefined by restrictions of the connection structure or the neutral fiber.

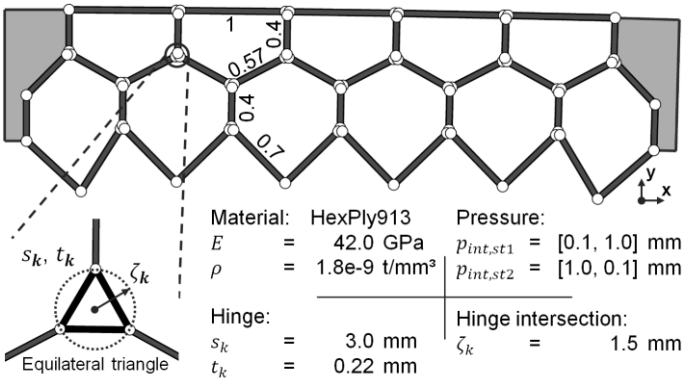

Figure 33: Initial settings for form-finding procedure of variable-camber wing PACS device

Table 4: Point loads at right hand connection structure

	Point load vectors $f_{pl,k}$ [N/m]			
	st1		st2	
$k = [h,i,j]$	x-comp	y-comp	x-comp	y-comp
[1,5,3]	-0.831	-4.528	-11.309	425.137
[1,5,5]	-0.575	-0.050	-267.899	-7.511

Table 5: Aerodynamic pressure loads for both states of shape

	Aerodynamic pressure $p_{ad,k}$ at cell side *j* [Pa]					
	st1			st2		
Number of cell *i*	h=1	1	2	10	1	2	10
1	715.6	615.8	-	2884.3	2679.4	-
2	516.9	420.7	615.8	2492.6	2172.4	2679.4
3	322.9	217.4	420.7	1866.7	1412.3	2172.4
4	117.8	-6.2	217.4	966.1	546.7	1412.3
5	-152.3	-	-6.2	122.7	-	546.7

Table 6: Cell side lengths of initial configuration

	Cell side length a_k at cell side *j* [mm]					
Number of cell *i*	h=1	1	3	5	7	9	11
1	71.093	25.957	38.077	38.077	27.457	
2	69.794	25.957	38.077	38.077	-	
3	69.794	25.957	38.077	38.077	-	
4	69.794	25.957	38.077	38.077	-	
5	71.093	27.457	38.077	38.077	-	
	h=2	1	3	5	7	9	11
1	30.457	-	-	25.957	49.175	49.175
2	-	-	-	25.957	49.175	49.175
3	-	-	-	25.957	49.175	49.175
4	-	-	-	25.957	49.175	49.175
5	-	-	-	25.957	49.175	49.175
6	-	-	-	30.457	49.175	49.175

Table 7: Cell side lengths of optimized configuration, variables that are modified during optimization are marked in italics

	Cell side length a_k at cell side *j* [mm]					
Number of cell *i*	h=1	1	3	5	7	9	11
1	71.093	*24.263*	*34.285*	*37.127*	27.457	
2	69.794	*27.041*	*37.170*	*40.768*	-	
3	69.794	*27.382*	*37.221*	*37.452*	-	
4	69.794	*23.284*	*42.705*	*37.322*	-	
5	71.093	27.457	*38.363*	*35.874*	-	
	h=2	1	3	5	7	9	11
1	30.457	-	-	*15.797*	*43.146*	*43.126*
2	-	-	-	*22.454*	*45.088*	*45.094*
3	-	-	-	*23.186*	*46.907*	*46.939*
4	-	-	-	*22.026*	*47.044*	*47.024*
5	-	-	-	*15.377*	*44.561*	*44.763*
6	-	-	-	30.457	*42.918*	*42.890*

8 Literature

[1] Huber J. E. et al., The selection of mechanical actuators based on performance indices. *Proceedings of the Royal Society A: Mathematical, Physical and Engineering Sciences*, vol. 453, no. 1965. 1997 October: 2185-2205.

[2] Hollerbach et al., A comparative analysis of actuator technologies for robotics. In Cambridge. *The robotics review 2*. Cambridge: MIT Press Cambridge; 1992. 299-342.

[3] Ranzani T. et al., A bioinspired soft manipulator for minimally invasive surgery. *Bioinspiration & Biomimetics*, vol. 10, no. 3. 2015 May: Art.Nr. 035008.

[4] Ilievski F. et al., Soft robotics for chemists. *Angewandte Chemie - International Edition*, vol. 50, no. 8. 2011 February: 1890-1895.

[5] Guiducci et al., Pressurized honeycombs as soft-actuators: a theoretical study. *Journal of the Royal Society Interface*, vol. 11, no. 98. 2014 September: Art.Nr. 20140458.

[6] Zhang et al., A multiscale method for the numerical analysis of active response characterization of 3D nastic structures. *Smart Materials and Structures*, vol. 21, no. 8. 2012 July: Art.Nr. 085009.

[7] Lv J. et al., Shape and topology optimization for closed liquid cell materials using extended multiscale finite element method. *Structural and Multidisciplinary Optimization*, vol. 49, no. 3. 2014 March: 367-385.

[8] Lv J. et al., Multiscale method for mechanical analysis of heterogeneous materials with polygonal microstructures. *Mechanics of Materials*, vol. 56, 2013 January: 38-52.

[9] Lv J. et al., A multiscale co-rotational method for geometrically nonlinear shape morphing of 2D fluid actuated cellular structures. *Mechanics of Materials*, vol. 79, 2014 December: 1 - 14.

[10] Luo Q. et al., Adaptive pressure-controlled cellular structures for shape morphing I: Design and analysis. *Smart Materials and Structures*, vol. 33, no. 5. 2013 May: Art.Nr.: 055014.

[11] Vos R. et al., Pressure adaptive honeycomb: A novel concept for morphing aircraft structures. In *27th Congress of the International Council of the Aeronautical Sciences 2010*; 2010; Nice, France. 1792 - 1801.

[12] Barrett R. et al., Biomimetic FAA-certifiable, artificial muscle structures for commercial aircraft wings. *Smart Materials and Structures*, vol. 23, no. 7. 2014 July 17: Art.Nr. 074011.

[13] Barrett R. et al., Method and apparatus for pressure adaptive morphing structure. Europe, *EP 2,459,442*. 2012 June 6.

[14] Vos R. et al., Method and apparatus for pressure adaptive morphing structure. USA, *US 8,366,057*. 2013 February 5.

[15] Pagitz M. et.al., Pressure-actuated cellular structures. *Bioinspiration and Biomimetics*, vol. 7, no. 1. 2012 March: Art.Nr. 016007.

[16] Gramüller B. et al., PACS - Realization of an adaptive concept using pressure actuated cellular structures. *Smart Materials and Structures*, vol. 23, no. 11. 2014 November 1: Art.Nr.115006.

[17] Gramüller B. et al., Shape-variable seals for pressure actuated cellular structures. *Smart Materials and Structures*, vol. 24, no. 9. 2015 July: Art.Nr.: 095005.

[18] Pagitz M. et al., A modular approach to adaptive structures. *Bioinspiration and Biomimetics*, vol. 9, no. 4. 2014 December: 046005.

[19] Sanders B. et al., Aerodynamic performance of the smart wing control effectors. *Journal of Intelligent Material Systems and Structures*, vol. 15, no. 4. 2004 April: 293-303.

[20] Szodruch J., The influence of camber variation on the aerodynamics of civil transport aircraft. In *AIAA 23rd Aerospace Sciences Meeting*; 1985; Reno, Nevada. Code 6416.

[21] Stanewsky E., Aerodynamic benefits of adaptive wing technology. *Aerospace Science and Technology*, vol. 4, no. 7. 2000 October: 439-452.

[22] Thornton S.V., Reduction of structural loads using maneuver load control on the Advanced Fighter Technology Integration. Technical Memorandum. Edwards, California: NASA; 1993. Report No.: 4526.

[23] Pagitz M. et al., Compliant pressure actuated cellular structures. [Online].: *arXiv 1403.2197*; 2014 [cited 2015 January 01. Available from: http://arxiv.org/abs/1403.2197v1.

[24] Pagitz M. et al., Design of pressure actuated cellular structures. [Online]. 1403.4033v1: *arXiV*; 2014 [cited 2015 September 19. Available from: http://arxiv.org/abs/1403.4033v1.

[25] Gramüller B. et al., PACS: Numerical approach and evaluation of a concept for dimensioning pressure-actuated cellular structures. *CEAS Aeronautical Journal*, 2015 August 23: 1-14.

[26] Thill C. et al., Morphing skins. *The aeronautical journal*, vol. 112, 2008 March: Art.Nr.1129.

[27] Hövelmann A. et al., Aerodyamic characteristics of the SAGITTA diamond wing demonstrator configuration. In *Deutscher Luft- und Raumfahrtkongress*; 2012; Berlin.

[28] da Rocha-Schmidt L. et al., A shape variable gap cover concept for aerodynamic control surfaces based on shear deformation. In *63. Deutscher Luft- und Raumfahrtkongress*; 2014; Augsburg.

[29] Fritz A.H. et al., Fertigungstechnik. 9th ed. Springer-Verlag. Berlin: Springer-Verlag; 2006.

[30] Westkämper E. et al., Einführung in die Fertigungstechnik. Wiesbaden: Vieweg+Teubner; 2010.

[31] Wiedemann J., Leichtbau - Elemente und Konstruktion. 3rd ed. Springer-Verlag. Berlin: Springer-Verlag; 2007.

[32] Wittel H. et al., Roloff / Matek Maschinenelemente. Wiesbaden: Vieweg+Teubner Verlag; 2011.